The Astronomical Journal, 162:90 (24pp), 2021 September https://doi.org/10.3847/1538-3881/ac04ae

Understanding the Angular Momentum Evolution of T Tauri and Herbig Ae/Be Stars

Giovanni Pinzón[1], Jesús Hernández[2], Javier Serna[2], Alexandra García[1], Ezequiel Manzo-Martínez[2,3], Alexandre Roman-Lopes[4], Carlos G. Román-Zúñiga[2], Maria Gracia Batista[1], Julio Ramírez-Vélez[2], Yeisson Osorio[5,6], and Ronald Avendaño[1]

[1] Observatorio Astronómico Nacional, Facultad de Ciencias, Universidad Nacional de Colombia, Bogotá, Colombia; gapinzone@unal.edu.co
[2] Universidad Nacional Autónoma de México, Instituto de Astronomía, AP 106, Ensenada 22800, Baja California, México
[3] Mesoamerican Centre for Theoretical Physics, Universidad Autónoma de Chiapas, Carretera Zapata Km. 4, Real del Bosque (Terán), Tuxtla Gutiérrez 29040, Chiapas, México
[4] Department of Astronomy—Universidad de La Serena—Av. Juan Cisternas, 1200 North, La Serena, Chile
[5] Instituto de Astrofísica de Canarias, E-38205 La Laguna, Tenerife, Spain
[6] Departamento de Astrofísica, Universidad de La Laguna (ULL), E-38206 La Laguna, Tenerife, Spain
Received 2021 February 1; revised 2021 May 11; accepted 2021 May 23; published 2021 August 5

Abstract

We investigate a sample of six Herbig Ae/Be stars belonging to the Orion OB1 association, as well as 73 low-mass objects, members of the σ Orionis cluster, in order to explore the angular momentum evolution at early stages of evolution, and its possible connection with main-sequence Ap/Bp magnetic stars. Using FIES and HECTOCHELLE spectra, we obtain projected rotational velocities through two independent methods. Individual masses, radii, and ages are computed using evolutionary models, distance, and cluster extinction. Under the assumption that similar physical processes operate in both T Tauri and Herbig Ae/Be stars, we construct snapshots of the protostar's rotation against mass during the first 10 Myr with the aid of a rotational model that includes a variable disk lifetime, changes in the stellar moment of inertia, a dipolar magnetic field with variable strength, and angular momentum loss through stellar winds powered by accretion. We use these snapshots, as well as the rotational data, to infer a plausible scenario for the angular momentum evolution. We find that magnetic field strengths of a few kilo-Gauss at 3 Myr are required to match the rotational velocities of both groups of stars. Models with masses between 2 $M_\odot$ and 3 $M_\odot$ display larger angular momentum values by a factor of $\sim$3, in comparison to stars of similar spectral types on the main sequence. Even though some quantitative estimates on this dramatic decrease with age for Ap/Bp magnetic main-sequence stars are presented, the results obtained for the angular momentum evolution do not explain their low rotation rates.

Unified Astronomy Thesaurus concepts: Stellar rotation (1629); Stellar properties (1624); Young stellar objects (1834); T Tauri stars (1681); Herbig Ae/Be stars (723); Protostars (1302); Pre-main sequence stars (1290); Stellar accretion disks (1579); Interstellar magnetic fields (845)

1. Introduction

The angular momentum evolution of pre-main-sequence (PMS) stars is mainly affected by internal processes that determine the angular momentum redistribution throughout the stellar interior (MacGregor & Brenner 1991; Moss 1992; Garaud 2020), as well as external processes such as stellar winds (Hayashi et al. 1996; Cranmer 2008) and the interaction between the star and the protoplanetary disk (Armitage & Clarke 1996; Matt & Pudritz 2005; Romanova et al. 2005; Matt et al. 2012; Gallet & Bouvier 2013, 2015; Li et al. 2014), all of them natural products of angular momentum conservation during the gravitational collapse of dense cores into protostars (Hartmann et al. 1998). In the current magnetospheric accretion scenario (MA), low-mass ($\leqslant 1.5\,M_\odot$) T Tauri stars (TTs) have their own magnetic field that truncates the disk at a few stellar radii from the star surface. From such a location, gas from the disk with higher angular momentum falls onto the star along the magnetic field lines during the so-called accretion phase. The energy released during accretion may excite large fluxes of Alfvén waves along open field lines in the magnetosphere, that is, stellar winds, which play an important role in the outward transfer of angular momentum (Boehm & Catala 1994; Corcoran & Ray 1997; Matt & Pudritz 2008). While this scenario describes angular momentum in TTs, its extrapolation toward intermediate-mass stars is not straightforward. The main dilemma is that only a small fraction of intermediate-mass (B and A) stars exhibit significant magnetic fields (Wade et al. 2007). However, several spectropolarimetric studies confirm the presence of weak fields in a number of Herbig Ae/Be stars (Hubrig et al. 2006; Alecian et al. 2008, 2013). In addition, the interplay between stellar accretion, winds, and protostellar disks in intermediate-mass stars is still matter of debate. There is evidence suggesting that more massive stars accrete material from their disks in different ways to that predicted by MA theory (Cauley & Johns-Krull 2014, 2015). However, recent findings indicate that MA may still operate in intermediate-mass pre-main-sequence stars such as HQ Tau (Pouilly et al. 2020). Furthermore, a trend between the strength of the longitudinal magnetic field and the accretion rate discussed in the work of Hubrig et al. (2009b) qualitatively supports the MA scenario for Herbig Ae/Be stars.

Herbig Ae/Be stars (hereafter HAeBes) are young stellar objects with masses between 1.5 $M_\odot$ and 10 $M_\odot$ that share characteristics with TTs despite differences in their stellar masses and internal structures. Both groups exhibit similar ages, infrared and ultraviolet excesses above the photosphere, and signs of magnetic activity, and some display P Cygni absorption features that originate in strong collimated winds (Hubrig et al. 2014; Wichittanakom et al. 2020). The internal structure of HAeBes differs from that of TTs; while the former is mainly radiative, TTs are mostly fully convective

(Iben 1965). This fact has a tremendous impact on the magnetic field generation and situates HAeBes as excellent candidates for testing the mass dependence of the MA scenario, in particular, regardless of whether they constitute a scaled version of TTs or not.

Despite lacking outer convective zones required to power a solar-type dynamo as observed in TTs (Moss 1984) almost ∼10% of the HAeBes exhibit predominantly dipolar magnetic fields with strengths between tens and thousands of Gauss (Alecian et al. 2013). These fields inferred from circular polarization measurements of selected line profiles are similar to those found in the peculiar (Ap/Bp) main-sequence stars, which are slow rotators with periods in the range from days to decades (Zorec & Royer 2012). This similarity can be interpreted as evidence supporting the idea that HAeBes are progenitors of the Ap/Bp stars. It has been suggested that Ap/Bp stars do not undergo significant angular momentum losses during the main-sequence phase and that any loss of angular momentum must occur either in the PMS phase or at the beginning of the main-sequence life, before the stars become observably magnetic (North 1998; Hubrig et al. 2000; Kochukhov & Bagnulo 2006). Rosen et al. (2012) carried out numerical simulations of the angular momentum evolution of accreting massive stars. They used a magnetically controlled scenario to demonstrate that the magnetic star–disk interaction's torques alone are insufficient to spin down massive young stars. This implies that other sources of angular momentum loss, such as stellar winds, must be taken into account. It also confirms that intermediate-mass stars lose angular momentum during their PMS stage under similar mechanisms to those operating in their lower mass counterparts (Aurière et al. 2007).

A better understanding of the angular momentum distribution as a function of spectral type can be achieved by using the results of multiepoch spectroscopic large surveys, such as Gaia-ESO[7] ($\geqslant 10^5$ stars) and the Sloan Digital Sky Survey (SDSS) V[8] ($\geqslant 6\times 10^6$ stars). These surveys provide stellar parameters, including stellar rotation measurements with high accuracy. Careful comparisons of projected rotational velocities ($v \sin i$) from both the literature and synthetic values are highly needed. In this sense, global rotational models of young stars capable of predicting trends between rotation, spectral types, accretion, and magnetic field for a large number of objects are necessary.

In this work we use a rotational model to search for trends between rotation, mass, stellar magnetic fields, and ages of TTs and HAeBes. We implement the magnetospheric accretion model of TTs toward higher and lower stellar masses in order to describe the angular momentum evolution for both mass regimes. For these purposes, we consider an approximately coeval sample of young stellar objects containing both TTs and HAeBes. We selected HAeBes members of the young Orion OB1 association, particularly from the subgroups *a* and *bc* (Hernández et al. 2005, 1–7 Myr;), and confirmed TTs members from the σ Orionis cluster (∼3 Myr; Hernández et al. 2007). We use this sample to study the interplay between rotation, the accreting disk, and stellar winds in intermediate-mass stars.

The paper is organized as follows. In Section 2, we describe the sample selection and observations. Stellar parameters are presented in Section 3, while in Section 4, we discuss the main features of rotation of TTs and HAeBes. The interplay between winds and accretion in HAeBes is described in Section 5, whereas synthetic $v \sin i$–mass relations and the angular momentum of HAeBes are discussed in Sections 6 and 7, respectively. In Section 8, we present a summary and our conclusions.

2. Sample Selection and Observations

2.1. The FIES Echelle Spectra

We selected five HAeBe stars located in the Orion OB1 association identified by Hernández et al. (2005) using the following criteria: (1) Hα in emission, (2) location in the HAeBe region of the *JHK* color–color diagram, and (3) strong IRAS 12 μm fluxes (Vieira et al. 2003). Two of the HAeBe stars are located in the Orion OB1a association (age ∼7–10 Myr) and the other three are located in the Orion OB1bc association (age ∼3–5 Myr). We also included the star HIP26500, which has an uncertain status between classical Be (CBe) star and HAeBe star (Hernández et al. 2005). Since HIP26500 has Hα in emission and significant infrared excesses (e.g., Chen et al. 2016; Vioque et al. 2018), we list this object as a HAeBe star.

We acquired high-resolution spectra of these six HAeBes (hereafter the HAeBe sample) and two comparison stars (HD87737 and HD53244) with the Fibre-fed Echelle Spectrograph (FIES[9]) on the Nordic Optical 2.5 m telescope (NOT) on 2014 January 20. FIES enables a resolution of 68,000 in the wavelength range of 3680–7270 Å. Exposure times were 400 s. Spectra were processed with the FIES pipeline FIEStools following typical reduction steps for echelle data, such as bias subtraction, flat-field normalization, extraction of the spectra, and assignment of wavelengths along the spectra. The stars HIP26752 and HIP25258 are spectroscopic binary systems (e.g., Vioque et al. 2018). We acquired spectroscopic data for the two components of the system HIP25258, which have an angular separation of ∼2ʺ.3. Since the angular separation of the components of the system HIP26752 is smaller than 2ʺ (Wheelwright et al. 2010), we have obtained FIES spectra for the combined stellar system.

Table 1 lists identifier, coordinates, spectral type, effective temperature ($T_{\rm eff}$), visual extinction ($A_{\rm V}$), and location reported by Hernández et al. (2005) for our sample. Table 1 also shows distances estimated from Gaia-EDR3 parallaxes (Gaia Collaboration 2020); since uncertainties for all our sources are smaller than 5%, we can apply the inverse relation between distance and parallax (Bailer-Jones 2015). For comparison, we also show the distances estimated by Briceño et al. (2019) for the subassociations Orion OB1a and Orion OB1b. The star HIP27059 is located in the spatial limit between the Orion OB1a and the Orion OB1b associations and has a distance similar to young stellar populations located in the Orion OB1a association (Pérez-Blanco et al. 2018; Briceño et al. 2019). Thus, it is probable that HIP27059 belongs to the Orion OB1a association instead of the Orion OB1b, as previously reported by Hernández et al. (2005). In Table 2 we show properties of the template spectra used for radial velocity and rotational measurements that were

[7] https://www.cosmos.esa.int/web/gaia
[8] https://www.sdss.org/future/

[9] Observations made with the Nordic Optical Telescope, operated by the Nordic Optical Telescope Scientific Association at the Observatorio del Roque de los Muchachos, La Palma, Spain, of the Instituto de Astrofisica de Canarias.

Table 1
Properties of the HAeBes Sample

HIP	HD	R.A.	Decl.	log[T_{eff} (K)][a]	SpT[a]	A_V (mag)[a]	OB1	d (pc)[a]	Gaia Distance (pc)[b]
26752	37806	05 41 02.29	−02 43 0.7	4.01	B9	0.21 ± 0.18	bc	400	397 ± 4
25299	287841	05 24 42.80	+01 43 48.2	3.88	A8	0.0 ± 0.42	a	360	336 ± 2
25258	287823	05 24 08.05	+02 27 46.9	3.94	A3	0.45 ± 0.23	a	360	343 ± 3
26500	37371	05 38 09.90	−00 11 1.2	3.95	A2	0.23 ± 0.22	bc	400	405 ± 5
26955	38120	05 43 11.89	−04 59 49.9	3.98	A0	0.13 ± 0.26	bc	400	381 ± 5
27059	38238	05 44 18.7	+00 08 40.41	3.87	A9	0.37 ± 0.27	a	400	323 ± 3

Notes. Columns 1 and 2 shows the target names, columns 3 and 4 are the R.A. and decl., respectively, column 5 is the log T_{eff}, column 6 is the spectral type, column 7 is the visual extinction, column 8 gives the OB1 subgroup, and column 9 is the distance reported by Briceño et al. (2019), whereas column 10 is the distance from Gaia-EDR3.
[a] Briceño et al. (2019).
[b] Gaia Collaboration (2020).

Table 2
Standard Stars Properties

HIP	HD	R.A.	Decl.	log[T_{eff} (K)]	SpT	RV (km s^{-1})[b]	$v \sin i$ (km s^{-1})	Gaia Distance (pc)[d]
49583	87737	10 07 19.95	+16 45 45.5	3.99	A0Ib	+3.3	23[a]	556 ± 92
34045	53244	07 03 45.49	−15 37 59.8	4.13	B8II	+32	36[c]	132 ± 4

Notes. Columns 1 and 2 correspond to identifiers, columns 3 and 4 are the R.A. and decl., column 5 is the log T_{eff}, column 6 is the spectral type, column 7 is the heliocentric radial velocity;, column 8 is the projected rotational velocity, and column 9 is the Gaia-EDR3 distance.
[a] Royer et al. (2002).
[b] Duflot et al. (1995).
[c] Simón-Díaz et al. (2017).
[d] Gaia Collaboration (2020).

selected from the radial velocities catalog of de Bruijne & Eilers (2012).

2.2. The Hectochelle Spectra

Using spectra obtained with the Hectochelle fiber-fed multiobject echelle spectrograph at the 6.5 m Telescope of the MMT Observatory (MMTO), Hernández et al. (2014) reported radial velocity (RVs), Hα, and Li I measurements for 142 stars in the σ Orionis cluster. These spectra have a resolution of 34,000 with 180 Å of spectral coverage centered at 6625 Å. From this data set, we complemented our study determining projected rotational velocities for 73 confirmed members that exhibit Li I in absorption (hereafter the TTs sample; see Section 3.3).

3. Stellar Parameters

3.1. Stellar Masses, Ages, and Radii

Based on previous estimations of spectral type and visual extinction given by Hernández et al. (2005) for the HAeBes sample and by Hernández et al. (2014) for the TTs sample, we computed effective temperatures (T_{eff}) by interpolating the spectral types using the standard table given by Pecaut & Mamajek (2013) for pre-main-sequence stars. Subsequently, we determined stellar luminosities based on the 2MASS J band, the Gaia-EDR3 parallaxes[10], and the extinction law of Cardelli et al. (1989). Finally, we computed stellar masses and ages by comparing the position of the stars in the H–R diagram with evolutionary models through the use of the code *MassAge* (J. Hernández et al. 2021, in preparation). This code generates for each star 300 artificial points, considering the values and uncertainties of the extinctions, spectral types, J magnitudes, and parallaxes. We selected the stellar mass and age of the closest theoretical point in the MIST evolutionary model grid for each artificial point.

We report the median value of age and mass for each star. The upper and lower limits correspond to the 1σ levels, where 68% of the individual results are included. In Figure 1, we compare the stellar masses derived from MIST (Dotter 2016) and Siess et al. (2000). In general, stellar masses are the same within the uncertainties. Stellar radii were obtained from the luminosity equation. For the HIP25258 binary system, whose components have similar parallaxes but quite different magnitudes, we estimate stellar parameters for the principal component. Masses, ages, and radii for the TTs are listed in Table 3 and those for the HAeBes in Table 4.

3.2. Radial Velocities

Radial velocities (RVs) for the HAeBes sample were computed using the IRAF task FXCOR, through a cross-correlation function (hereafter, CCF) that compares each star with a synthetic or empirical template with similar spectral type, corrected by radial velocity. Each object's spectrum was cross-correlated with its respective template in the spectral window 4480 Å $< \lambda <$ 4600 Å. Subsequently, the quality of the cross-correlation was measured through the parameter R, defined as the signal-to-noise ratio (S/N) of the cross-correlation function (Tonry & Davis 1979). Heliocentric radial velocities in Table 4 are those that give the highest R values. Uncertainties were computed through the R parameter as $\sigma_v = v_{rad}/(1 + R)$.

For five of our HAeBes stars, Alecian et al. (2013) measured RVs found through fitting of LSD Stokes I profiles obtained

[10] The parallax uncertainties in Gaia-EDR3 are below 20% for this sample; therefore, we can apply this inverse relation (Bailer-Jones 2015).

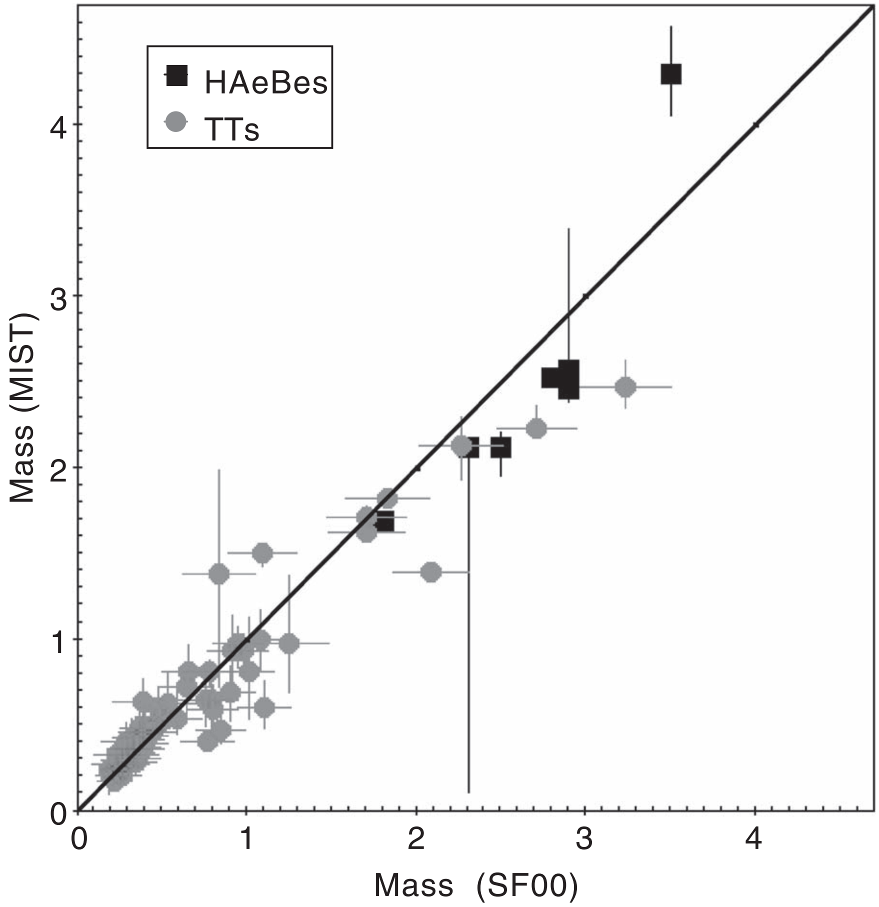

Figure 1. Comparison between the stellar masses derived through the *MassAge* code using evolutionary models of MIST (Dotter 2016) and the SF00 models (Siess et al. 2000) for our sample. TTs are confirmed members of σ Orionis with Li I in absorption. The MIST mass of the HAeBe binary HIP25258 corresponds to the principal component (see the text).

with the high-resolution spectropolarimeters ESPaDOnS and Narval at the CFHT and Bernard Lyot Telescope, respectively. The most prominent difference between our results and those reported by the authors occur for the star HIP26752, which has the biggest reported error bar. For the spectroscopic binary HIP25258, we fit a deblending function using the Levenberg–Marquardt method with initial values determined by the line centers obtained with FXCOR. Differences with other studies are likely due to observations carried out in different epochs, which is expected to cause variations in the RVs of binary system components.

Heliocentric radial velocities (RVs) for the σ Orionis cluster were estimated by Hernández et al. (2014, see Table 5) using the IRAF package RVSAO that cross-correlates each observed spectrum with a set of synthetic solar metallicity stellar templates from Coelho et al. (2005). The authors reported a list of binary candidates that either exhibit double peaks in the cross-correlation functions or present strong RV variability. In Table 3 we labeled these objects with “b” and “c,” respectively. Except for those objects, the TTs sample can be considered to be formed by single objects.

3.3. Rotational Velocities

Projected rotational velocities ($v \sin i$) for TTs and HAeBes were obtained applying two methods: (1) analysis of the cross-correlation function of the object spectrum against a rotational template (Tonry & Davis 1979; Hartmann et al. 1986) and (2) Fourier Transform (FT) of selected line profiles in the object spectrum (J. Serna et al. 2021, in preparation).

3.3.1. Cross-correlation Function Analysis

In the CCF-based method, the $v \sin i$ of the star is obtained through the calculation of the cross-correlation function of each object against a stellar template of similar spectral type artificially broadened at different velocities. This manufactured broadening was done by using the Python routine *rotbroad* of the *PyAstronomy* package with a solar limb-darkening coefficient of $\epsilon = 0.6$ (Ramanathan 1954; Hartmann et al. 1986). For each broadening velocity, we fitted the peak of the cross-correlation function with a parabola and measured its FWHM and its S/N through the TDR parameter (Tonry & Davis 1979). Rotational projected velocity is given by the minimum value of the FWHM of the parabola that better fits the peak of the CCF by a calibration function (Sacco et al. 2008). This function is computed from a template–template CCF, which is broadened in 2 km s^{-1} steps. The procedure is carried out on the spectral window (6580 Å $< \lambda <$ 6700 Å), suppressing any emission feature in the observed spectra before the correlation is computed.

For the Hectochelle sample (i.e., the TTs), we used synthetic templates from the LTE static parallel line-blanketed ATLAS9 model of Kurucz (1979). We assumed solar metallicity and a range of surface gravities $4.0 < \log\ g < 5.0$ and effective temperatures 3500 K $< T_{\rm eff} <$ 5000 K, depending on the

Table 3
Derived Stellar Parameters for Confirmed Members in the σ Orionis Cluster Reported by Hernández et al. (2014) and with Errors in Gaia-EDR3 Parallaxes Below 20%

2MASS ID	$T_{\rm eff}$ (K)	$M/M_\odot$	Age ($\times10^6$ y)	$R/R_\odot$	SpT[a]	$v \sin i^{\rm CCF}$ (km s^{-1})	$v \sin i^{\rm Fourier}$ (km s^{-1})	Acc?
05393511-0247299	4268 ± 256	$0.93^{0.20}_{-0.20}$	$3.09^{6.92}_{-1.82}$	1.58 ± 0.13	K5.5	43 ± 2.7	43.5 ± 1.7	⋯
05380649-0228494	6665 ± 279	$1.82^{0.03}_{-0.04}$	$6.76^{7.24}_{-6.17}$	2.72 ± 0.18	F3.5	55 ± 9	59.3 ± 1.4	⋯
05400696-0228300	6231 ± 181	$1.39^{0.03}_{-0.03}$	$12.88^{13.49}_{-11.48}$	1.79 ± 0.09	F7.5	17.1 ± 4	15 ± 6	⋯
05385911-0247133	3711 ± 101	$0.40^{0.04}_{-0.03}$	$0.13^{0.19}_{-0.13}$	3.17 ± 0.20	M2.0	24.2 ± 3.3	21.6 ± 4.5	⋯
05393654-0242171	5935 ± 135	$2.47^{0.15}_{-0.12}$	$2.51^{3.02}_{-2.04}$	4.11 ± 0.17	G1.0	200 ± 10	196.7 ± 3.05	⋯
05374963-0236182	5855 ± 323	$2.13^{0.17}_{-0.20}$	$3.55^{5.13}_{-2.40}$	3.17 ± 0.26	G2.5	<9.0	10.5 ± 3.5	⋯
05375440-0239298	5780 ± 146	$2.23^{0.13}_{-0.05}$	$3.09^{3.31}_{-2.34}$	3.30 ± 0.14	G5.0	23.3 ± 0.6	21.2 ± 3.2	⋯
05391717-0225433	3645 ± 120	$0.46^{0.11}_{-0.09}$	$2.63^{4.37}_{-2.00}$	1.27 ± 0.09	M1.5	<9.0	14.1 ± 8.5	⋯
05372831-0224182	3477 ± 120	$0.35^{0.08}_{-0.06}$	$18.62^{25.70}_{-14.13}$	0.62 ± 0.04	M3.0	<9.0	11.1 ± 3.9	Y
05373666-0234003	3471 ± 56	$0.35^{0.04}_{-0.03}$	$4.37^{5.01}_{-3.72}$	1.00 ± 0.03	M3.0	33.8 ± 5.6	34.1 ± 10	Y
05373784-0245442	3578 ± 68	$0.41^{0.05}_{-0.04}$	$2.46^{3.02}_{-2.14}$	1.30 ± 0.05	M2.0	23.5 ± 0.4	20.1 ± 4	N
05374527-0228521	3303 ± 138	$0.25^{0.07}_{-0.08}$	$5.50^{8.71}_{-2.82}$	0.81 ± 0.05	M4.5	⋯	16.5 ± 3.7	Y
05375161-0235257	3579 ± 62	$0.39^{0.04}_{-0.03}$	$1.05^{1.20}_{-0.98}$	1.73 ± 0.06	M2.0	34.9 ± 4.6	36.5 ± 1.4	N
05375404-0244407	3485 ± 242	$0.35^{0.17}_{-0.14}$	$3.02^{5.50}_{-1.55}$	1.16 ± 0.12	M3.0	23.3 ± 0.6	21.2 ± 3.2	N
05380055-0245097	3237 ± 79	$0.21^{0.04}_{-0.04}$	$1.32^{1.62}_{-1.05}$	1.29 ± 0.05	M5.0	47 ± 6.1	44 ± 2.4	Y
05380897-0220109	3424 ± 55	$0.32^{0.03}_{-0.03}$	$3.47^{4.07}_{-2.88}$	1.05 ± 0.04	M3.5	⋯	18.6 ± 4.3	Y
05381718-0222256	3233 ± 80	$0.21^{0.04}_{-0.04}$	$3.39^{4.79}_{-2.24}$	0.88 ± 0.04	M5.0	<9.0	6.9 ± 3.8	Y
05382354-0241317	3310 ± 72	$0.25^{0.05}_{-0.04}$	$3.16^{4.17}_{-2.29}$	0.98 ± 0.04	M4.5	<9.0	12.9 ± 2.2	Y
05382774-0243009	3460 ± 106	$0.33^{0.07}_{-0.05}$	$1.02^{1.18}_{-0.85}$	1.67 ± 0.09	M3.0	29.1 ± 3.8	26.7 ± 1.4	Y
05383284-0235392	4206 ± 162	$0.81^{0.15}_{-0.13}$	$1.48^{2.19}_{-1.05}$	1.91 ± 0.10	K6.0	22.8 ± 4.2	23.6 ± 0.4	N
05383546-0231516	4044 ± 178	$0.64^{0.16}_{-0.15}$	$0.85^{1.32}_{-0.56}$	2.14 ± 0.13	K7.0	21.9 ± 2.9	23.4 ± 0.4	N
05383745-0250236	3302 ± 186	$0.24^{0.11}_{-0.10}$	$1.59^{2.51}_{-0.34}$	1.27 ± 0.11	M4.5	25.9 ± 7.4	23.7 ± 8	Y
05384008-0250370	3288 ± 122	$0.24^{0.08}_{-0.06}$	$3.98^{6.17}_{-2.46}$	0.88 ± 0.06	M4.5	<9.0	8.3 ± 3.7	Y
05384129-0237225	3855 ± 168	$0.53^{0.17}_{-0.08}$	$0.85^{1.32}_{-0.65}$	2.04 ± 0.12	M0.0	14.5 ± 1.5	17.9 ± 1.5	N
05384355-0233253	3674 ± 207	$0.46^{0.16}_{-0.11}$	$1.51^{2.88}_{-1.05}$	1.56 ± 0.14	M1.5	19 ± 4	21.6 ± 1.7	N
05384993-0241228	3458 ± 114	$0.34^{0.08}_{-0.06}$	$2.24^{2.75}_{-1.78}$	1.25 ± 0.07	M3.0	23.1 ± 4.5	21.4 ± 3.5	N
05385317-0243528	3712 ± 148	$0.48^{0.12}_{-0.08}$	$1.41^{2.09}_{-1.05}$	1.65 ± 0.09	M1.0	19.5 ± 2.1	23.1 ± 0.5	N
05385831-0216101	3850 ± 94	$0.60^{0.13}_{-0.05}$	$2.69^{3.63}_{-2.19}$	1.44 ± 0.06	M0.0	21 ± 3.1	23.6 ± 0.5	N
05390276-0229558	3371 ± 123	$0.28^{0.06}_{-0.08}$	$1.62^{2.14}_{-1.15}$	1.31 ± 0.08	M4.0	20.1 ± 2.5	19.3 ± 0.9	N
05390853-0251465	3776 ± 74	$0.51^{0.05}_{-0.04}$	$1.26^{1.62}_{-1.07}$	1.74 ± 0.08	M0.5	⋯	22.7 ± 0.6	N
05392286-0233330	3594 ± 120	$0.42^{0.10}_{-0.07}$	$2.63^{3.89}_{-2.09}$	1.27 ± 0.07	M2.0	<9.0	14.5 ± 2.9	N
05392456-0220441	4175 ± 319	$0.81^{0.32}_{-0.28}$	$1.86^{4.47}_{-0.89}$	1.77 ± 0.18	K6.0	51.9 ± 5.1	53.2 ± 2.8	N
05392650-0252152	3367 ± 59	$0.29^{0.03}_{-0.04}$	$2.57^{3.09}_{-2.04}$	1.11 ± 0.04	M4.0	22.4 ± 3.5	18 ± 1	Y
05393291-0247492	3782 ± 70	$0.50^{0.04}_{-0.04}$	$0.93^{1.10}_{-0.79}$	1.93 ± 0.06	M0.5	31.6 ± 2.8	27.2 ± 7.8	N
05393729-0226567	3964 ± 168	$0.62^{0.18}_{-0.13}$	$1.18^{1.91}_{-0.81}$	1.89 ± 0.11	K7.5	28.6 ± 4	29.6 ± 3.2	N
05382119-0254110	3148 ± 90	$0.17^{0.05}_{-0.03}$	$1.32^{1.78}_{-0.49}$	1.21 ± 0.05	M5.5	10.2 ± 2.3	17.2 ± 0.6	Y
05385410-0249297[b]	5080 ± 256	$1.51^{0.03}_{-0.08}$	$4.68^{6.76}_{-2.40}$	1.95 ± 0.15	K1.0	31 ± 2	29.1 ± 0.6	N
05391163-0236028[b]	4077 ± 167	$0.72^{0.13}_{-0.19}$	$1.62^{2.24}_{-0.98}$	1.77 ± 0.10	K7.0	⋯	⋯	N
05393256-0239440[b]	4053 ± 170	$0.60^{0.15}_{-0.12}$	$0.42^{0.59}_{-0.32}$	2.74 ± 0.16	K7.0	29.9 ± 7.1	35.2 ± 3.1	N
05384027-0230185[b]	4057 ± 159	$0.64^{0.14}_{-0.12}$	$0.68^{0.96}_{-0.49}$	2.31 ± 0.12	K7.0	21 ± 1.6	17.7 ± 1.7	N
05375486-0241092	3239 ± 84	$0.21^{0.04}_{-0.05}$	$3.09^{4.27}_{-2.09}$	0.91 ± 0.04	M5.0	<9.0	8.2 ± 2.7	Y
05381886-0251388	3530 ± 119	$0.38^{0.07}_{-0.06}$	$2.19^{2.88}_{-1.74}$	1.31 ± 0.08	M2.5	<9.0	13.2 ± 2.4	N
05384423-0240197	4208 ± 71	$0.81^{0.07}_{-0.08}$	$1.41^{1.70}_{-1.15}$	1.95 ± 0.05	K6.0	22.6 ± 3.2	23.4 ± 0.6	N
05382911-0236026	3659 ± 63	$0.46^{0.04}_{-0.05}$	$2.19^{2.63}_{-1.82}$	1.39 ± 0.04	M1.5	⋯	23.3 ± 0.6	N
05383431-0235000	4054 ± 170	$0.65^{0.14}_{-0.15}$	$0.81^{1.20}_{-0.55}$	2.16 ± 0.12	K7.0	32.4 ± 3.1	31.9 ± 0.8	N
05373094-0223427	3585 ± 61	$0.42^{0.06}_{-0.04}$	$3.89^{4.90}_{-3.47}$	1.11 ± 0.04	M2.0	18.4 ± 6.5	21.1 ± 2	Y
05380107-0245379[b]	3307 ± 66	$0.25^{0.04}_{-0.03}$	$1.91^{2.46}_{-1.55}$	1.16 ± 0.06	M4.5	27.9 ± 7.5	30.3 ± 1.4	Y
05380674-0230227	3867 ± 89	$0.55^{0.08}_{-0.06}$	$1.07^{1.35}_{-0.87}$	1.89 ± 0.07	M0.0	16.6 ± 2.1	20.3 ± 1.2	Y
05380994-0251377	3473 ± 50	$0.31^{0.02}_{-0.02}$	$0.13^{0.13}_{-0.13}$	2.78 ± 9.56	M3.0	<9.0	9.9 ± 3.5	Y
05381315-0245509	3660 ± 66	$0.43^{0.04}_{-0.04}$	$1.05^{1.20}_{-0.89}$	1.77 ± 0.05	M1.5	23.1 ± 0.5	21.1 ± 3.1	Y
05381319-0226088	3361 ± 124	$0.27^{0.07}_{-0.07}$	$1.18^{1.74}_{-0.81}$	1.46 ± 0.13	M4.0	22.1 ± 0.7	19.2 ± 5.5	Y
05382050-0234089	3369 ± 124	$0.27^{0.05}_{-0.08}$	$0.74^{0.89}_{-0.21}$	1.83 ± 0.12	M4.0	24.4 ± 6.3	23.4 ± 0.5	Y
05382358-0220475	3362 ± 129	$0.29^{0.06}_{-0.10}$	$8.71^{16.98}_{-3.89}$	0.71 ± 0.11	M4.0	<9.0	11.9 ± 3.7	Y
05382543-0242412	3290 ± 222	$0.24^{0.11}_{-0.14}$	$16.22^{34.67}_{-3.89}$	0.54 ± 0.07	M4.5	<9.0	13.2 ± 2.3	Y
05382725-0245096	4210 ± 167	$0.93^{0.09}_{-0.15}$	$5.01^{7.59}_{-3.24}$	1.37 ± 0.07	K6.0	19.2 ± 2.7	21.9 ± 6.8	Y
05383368-0244141	4471 ± 261	$0.98^{0.40}_{-0.28}$	$0.54^{0.98}_{-0.29}$	2.97 ± 0.33	K4.5	24.2 ± 7.3	22.7 ± 0.6	Y
05384301-0236145	3716 ± 142	$0.47^{0.12}_{-0.07}$	$1.15^{1.74}_{-0.89}$	1.75 ± 0.10	M1.0	19 ± 4	22.9 ± 0.4	Y

Table 3
(Continued)

2MASS ID	$T_{\rm eff}$ (K)	$M/M_\odot$	Age ($\times 10^6$ y)	$R/R_\odot$	SpT[a]	$v \sin i^{\rm CCF}$ (km s^{-1})	$v \sin i^{\rm Fourier}$ (km s^{-1})	Acc?
05384537-0241594	3661 ± 212	$0.48^{0.19}_{-0.14}$	$3.89^{7.59}_{-2.34}$	1.16 ± 0.12	M1.5	…	22.5 ± 0.9	Y
05384718-0234368	3401 ± 191	$0.30^{0.09}_{-0.12}$	$1.35^{1.86}_{-0.44}$	1.43 ± 0.12	M4.0	<9.0	8.1 ± 3.7	Y
05390136-0218274	3780 ± 77	$0.49^{0.04}_{-0.04}$	$0.87^{1.02}_{-0.74}$	1.96 ± 0.06	M0.5	20.4 ± 3.2	19.7 ± 1	Y
05390297-0241272	3520 ± 53	$0.37^{0.03}_{-0.03}$	$1.29^{1.41}_{-1.15}$	1.58 ± 0.05	M2.5	22.9 ± 3	18.7 ± 1.4	Y
05390357-0246269	3426 ± 121	$0.32^{0.06}_{-0.08}$	$2.51^{3.09}_{-1.66}$	1.18 ± 0.07	M3.5	17 ± 4	20.4 ± 1.3	Y
05390878-0231115	3485 ± 116	$0.35^{0.06}_{-0.07}$	$2.29^{2.88}_{-1.74}$	1.26 ± 0.07	M3.0	14.5 ± 3.1	16.9 ± 2.7	Y
05393982-0231217	4265 ± 177	$0.97^{0.10}_{-0.15}$	$4.57^{7.59}_{-3.02}$	1.44 ± 0.08	K5.5	<9.0	15.1 ± 1.8	Y
05394017-0220480	4363 ± 189	$1.00^{0.18}_{-0.18}$	$2.88^{5.01}_{-1.74}$	1.68 ± 0.10	K5.0	21.7 ± 5.1	17.8 ± 0.6	Y
05400889-0233336	3948 ± 155	$0.59^{0.14}_{-0.11}$	$0.87^{1.29}_{-0.66}$	2.05 ± 0.11	K7.5	22.04 ± 4.1	17.6 ± 0.9	Y
05383460-0241087	3575 ± 123	$0.41^{0.11}_{-0.07}$	$2.00^{3.02}_{-1.70}$	1.37 ± 0.08	M2.0	<9.0	9.6 ± 2.2	Y
05380826-0235562	3524 ± 59	$0.36^{0.03}_{-0.04}$	$0.98^{1.07}_{-0.89}$	1.75 ± 0.06	M2.5	22.7 ± 4.5	22.8 ± 0.5	Y
05381412-0215597[c]	6260 ± 226	$1.72^{0.06}_{-0.02}$	$7.08^{7.76}_{-6.17}$	2.50 ± 0.16	F7.5	27.4 ± 9	29.1 ± 7.7	Y
05382684-0238460	3416 ± 122	$0.32^{0.06}_{-0.08}$	$7.59^{10.47}_{-4.79}$	0.79 ± 0.06	M3.5	19 ± 3	17.4 ± 1.3	Y
05383587-0243512	4729 ± 466	$1.38^{0.60}_{-0.66}$	$0.78^{2.82}_{-0.26}$	3.09 ± 0.44	K3.0	30.5 ± 1.2	26.4 ± 7.3	Y
05375303-0233344[b]	5899 ± 124	$1.62^{0.05}_{-0.05}$	$7.59^{8.13}_{-6.46}$	2.19 ± 0.07	G2.5	41.3 ± 2.5	46.4 ± 0.9	Y
05383587-0230433[b]	4067 ± 181	$0.68^{0.16}_{-0.16}$	$1.20^{1.74}_{-0.78}$	1.93 ± 0.12	K7.0	84.9 ± 9.3	89.3 ± 1.6	Y

Notes. Column 1 corresponds to the 2MASS identifier, column 2 is the effective temperature, and columns 3, 4, and 5 give mass, radius, and age, respectively. The spectral types are shown in column 6. The $v \sin i$ obtained through CCF analysis are shown in column 7, whereas those obtained from the Fourier analysis are indicated in column 8. Finally, the flag (Y/N) in column 9 corresponds to a previous classification based on an Hα line.
[a] Hernández et al. (2014).
[b] binary candidate identified by Hernández et al. (2014).
[c] binary candidate identified by Kounkel et al. (2019).

Table 4
Derived Stellar Parameters for the HAeBes Sample

HIP	RV (km s^{-1})	RV (km s^{-1})[a]	$v \sin i^{\rm CCF}$ (km s^{-1})	$v \sin i^{\rm Fourier}$ (km s^{-1})[b4]	$R/R_\odot$	$M/M_\odot$	Age (Myr)	$[3.4\text{–}12]_0$
26752	17 ± 1	47 ± 21	128 ± 7	120.7 ± 25.2	$5.5^{+0.7}_{-0.5}$	$4.3^{+0.2}_{-0.3}$	$0.85^{+0.1}_{-0.1}$	3.19
25299	19 ± 3	20.0 ± 3.6	118 ± 18	123.5 ± 9.0	$1.7^{+0.2}_{-0.1}$	$1.7^{+0.1}_{-0.1}$	$12.02^{+1.80}_{-11.47}$	2.13
25258A	−7.8 ± 0.3	−0.3 ± 1.1	10.3 ± 2.2	…	$2.0^{+0.0}_{-0.1}$	$2.1^{+0.2}_{-0.1}$	$6.46^{+0.6}_{-0.5}$	2.41
25258B	50.5 ± 2.4	54.0 ± 1.6	7.2 ± 0.3	…	$2.0^{+0.9}_{-0.1}$	$2.1^{+0.6}_{-0.2}$	$6.46^{+0.6}_{-0.5}$	2.41
26500	51 ± 15	…	116 ± 15	99.4 ± 5.7	$3.0^{+0.1}_{-0.1}$	$2.5^{+0.1}_{-0.1}$	$3.55^{+0.2}_{-0.2}$	1.37
26955	26.8 ± 4.7	28 ± 12	103 ± 5	97 ± 21	$3.0^{+0.0}_{-0.1}$	$2.6^{+0.1}_{-0.6}$	$3.31^{+0.8}_{-0.3}$	4.95
27059	16.9 ± 1.5	15.0 ± 2.9	119 ± 11	111.1 ± 16.8	$3.9^{+0.2}_{-0.1}$	$2.5^{+0.1}_{-0.1}$	$3.02^{+0.2}_{-0.2}$	1.91

Notes. Column 1 is the identifier, and column 2 is the radial velocity (RV) obtained from our CCF analysis. The RV reported by Alecian et al. (2013) is shown in column 3. The stellar rotation computed through CCF and Fourier techniques is shown in columns 4 and 5, whereas columns 6, 7, and 8 correspond to the stellar radius, mass, and age. The last column gives the WISE infrared intrinsic color [3.4–12] μm.
[a] Alecian et al. (2013).

Table 5
KS Statistic on Observed and Expected Samples of Specific Angular Momentum as a Function of Mass

	TTs		HAeBes	
B_* (kG)	KS	p-val	KS	p-val
0.5	0.60	…	0.85	0.001
1.0	0.54	0.002	0.47	0.240
2.0	0.20	0.712	0.33	0.631
3.0	0.35	0.102	0.74	0.008

Note. Expected J were obtained using $\tau_D = 3$ Myr. If KS is small or the p-val is high, then we cannot reject the hypothesis that the distributions of the two samples are the same.

spectral type reported by Hernández et al. (2014). The spectra were degraded to the Hectochelle instrument resolution before starting the broadening at steps of 2 km s^{-1}. As an example, the first panel of Figure 2(a) shows the $v \sin i$ determination for the K1 star 2MASS J05385410-0249297 (upper spectrum) using a template with $T_{\rm eff} = 4500$ K and $\log g = 4.5$ (lower spectrum). Through the use of the calibration function, the minimum of the CCF at 27 km s^{-1} leads to a $v \sin i = (31 \pm 2)$ km s^{-1}. Uncertainties in the CCF method depend on the errors in the correlation process and are calculated using the R parameter (see Section 3.2). In column 7 of Table 3 we report $v \sin i$ CCF measurements for TTs. Due to low S/N and uncertainties in the method, almost 30% of the sample exhibits the lowest measurable rotational velocity of $\sim$9 km s^{-1}, which corresponds to the instrumental broadening.

The FIES sample in the same spectral window is characterized by the absence of single lines with good S/N, which adds noise to the cross-correlation function. However, in contrast to other methods, CCF is able to deal with this fact, since all spectral features are included via a quadratic sum (Tonry & Davis 1979). For HAeBes, we constructed two

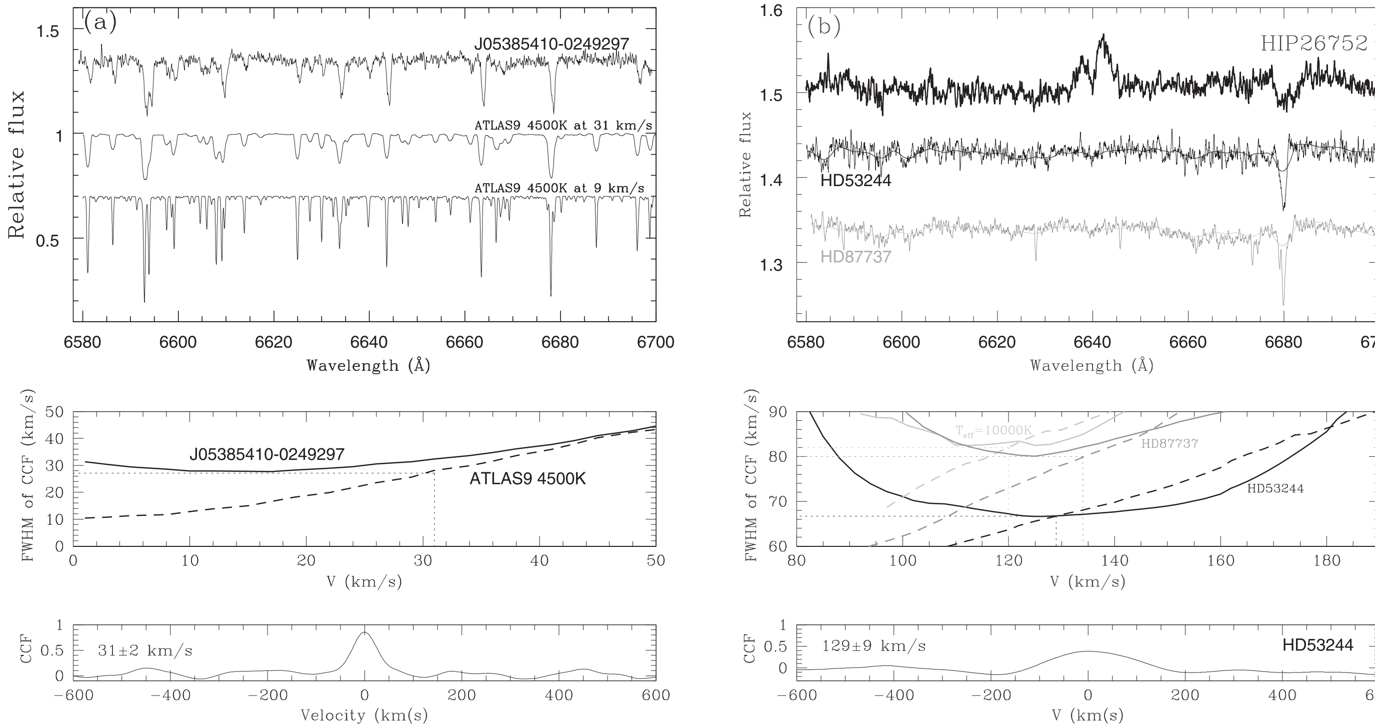

Figure 2. (a) The cross-correlation method applied on the TT star 2MASS J05385410-0249297 (SpT K1.0, upper spectrum). The synthetic stellar template (lower spectrum) is shown with its corresponding broadened spectrum in the middle. In the second panel, the FWHM between object and broadened template is indicated with a solid line, whereas the dashed line corresponds to the calibration function after interpolation with a third-order polynomial. The third panel illustrates the CCF corresponding to a broadening of 31 km s^{-1} which is the velocity that minimizes the width of the CCF using the calibration function. (b) Same technique applied to the HAeBe star HIP26752 (SpT B9, upper spectrum) using the spectra of HD53244 (SpT B8II, middle spectrum) and HD87737 (SpT A0Ib, lower spectrum in gray), observed during the same night, as stellar templates. Thin lines show the broadened spectra at the $v \sin i$ of the star. The middle panel shows the FWHM of the CCF between object and template with thick lines, whereas the dashed lines represents those computed with the templates HD53244 (black), HD87737 (dark gray), and a synthetic A0 star (light gray). Error bars in the final $v \sin i$ determination are computed using the R parameter; details are given in the text.

calibration functions with the observed templates listed in Table 2 and one with a synthetic spectrum (with spectral type A0; an ATLAS9 model of Kurucz 1979). Figure 2(b) illustrates the $v \sin i$ determination for the B9 star HIP26752, the most massive HAeBe star in our sample (upper spectrum in the first panel). Original and broadened stellar templates are plotted with thick and thin lines, respectively. In the middle panel, minima in the FWHM of the CCF were identified at 129 km s^{-1} for HD53244, 134 km s^{-1} for HD87737, and 125 km s^{-1} for the synthetic template. Using the calibration functions (dashed lines), we obtain a mean value $v \sin i = (128 \pm 7)$ km s^{-1} for HIP26752 computed with the three templates. For the particular case of the stellar template HD53244, the resultant CCF (bottom right panel) is slightly higher than the noise ($R = 3$). Despite showing chemical spots leading to rotational and radial velocity variability (Briquet et al. 2010), we obtain $v \sin i = (129 \pm 9)$ km s^{-1} using this star as a template. The fast rotation of HIP26752 that leads to a strong line blending seems to be the main source of broadening of the correlation peak, as pointed out in previous studies (Royer et al. 2002; Díaz et al. 2011). For the rest of HAeBes, we obtain the best results using HD87737 as a rotational template. The $v \sin i$ CCF values are shown in column 4 of Table 4.

3.3.2. Fourier Transform (FT) Analysis

Some limitations of the CCF method are: (1) the assumption that rotation is the dominant broadening process of the photospheric lines (Wilson 1969), (2) a strong dependence on the calibration function, and (3) variations in $v \sin i$ depending on the spectral window (Hartmann et al. 1986). These factors are avoided thanks to methods based on Fourier transform (FT) of selected line profiles. The method relies on the fact that the FT of the observed line has zeros whose location is related to the $v \sin i$ of the star. Specifically, if we denote with ν_1 the first zero of the FT of a line profile at λ_0, the resultant rotational projected velocity is given by $v \sin i = c\Delta\lambda/\lambda_0$ where $\Delta\lambda = \nu_1/q_1$; here ν_1 is the first zero of the FT and q_1 is a polynomial function that depends on the limb darkening (Carroll 1933). Under the assumption that TTs and HAeBes share same limb-darkening physics, we adopted $\epsilon = 0.6$ and subsequently $q_1 = 0.660$ in all calculations.

We applied this method to our studied sample as follows. For TTs we focused mainly on the Li 6707.74/89 Å doublet, which has good S/N in our Hectochelle spectra. For a few cases where the doublet is not present, or it is contaminated by the merging of spectral orders, we use the stellar spectral features Fe I 6575 Å, 6696 Å. We report rotational projected velocities for 72 objects using the FT method labeled as $v \sin i^{\rm Fourier}$ in Table 3. For HAeBes we applied FT to Mg II 4481 Å, Fe I 4489 Å, and Fe I 4226 Å line profiles, which have been tested as excellent rotational indicators in previous studies of stellar rotation. Values appearing in column 4 of Table 4 correspond to the average of the $v \sin i^{\rm Fourier}$ values obtained from all lines. Comparison with the CCF-based method is indicated with open squares in Figure 3. Absolute differences between Fourier and CCF methods remain below 5 km s^{-1} in

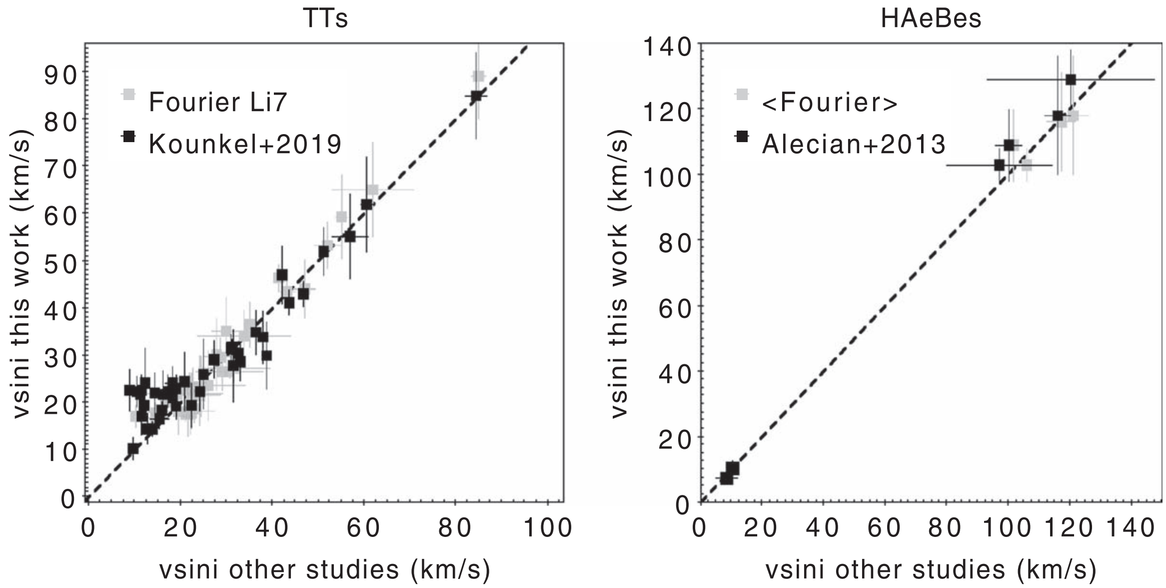

Figure 3. Left. Comparison of $v \sin i$ measurements using the CCF method with those obtained through FT applied to the Li 6707 Å absorption line (gray). Symbols in black correspond to a comparison with Kounkel et al. (2019). Right. Same comparison for HAeBes. Symbols in gray correspond to an average obtained from the FT method applied to the Mg II 4481 Å, Fe I 4226 Å, and Fe I 4489 Å lines. Symbols in black represent a comparison to $v \sin i$ reported by Alecian et al. (2013).

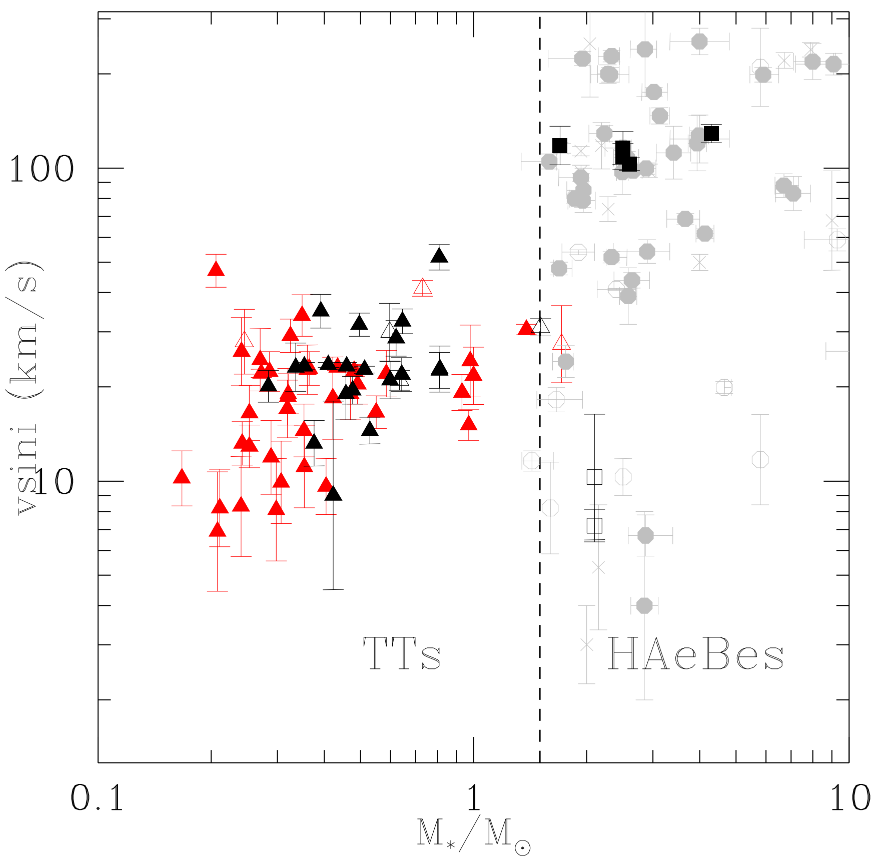

Figure 4. $v \sin i$ vs. stellar mass for TTs (triangles) and HAeBes (rectangles). TTs with active accretion reported by Hernández et al. (2014) are indicated with bigger triangles in red. Complementary data of HAeBes taken from Alecian et al. (2013) and Fairlamb et al. (2015) have been included in gray. Binaries are indicated with open circles and upper limit values with crosses.

the worst of the cases, and is slightly larger values for HAeBes. In view of the strong dependence of the CCF method with the calibration function, we find it reasonable to keep the $v \sin i^{\mathrm{Fourier}}$ estimates, instead of the upper values obtained from $v \sin i^{\mathrm{CFF}}$ in the TTs sample.

3.3.3. Comparison with Previous Studies

We compared the rotational velocities obtained through the CCF technique with those previously published. In the case of TTs, Sacco et al. (2008) conducted a similar study in σ Orionis based on FLAMES spectroscopic observations with the Very

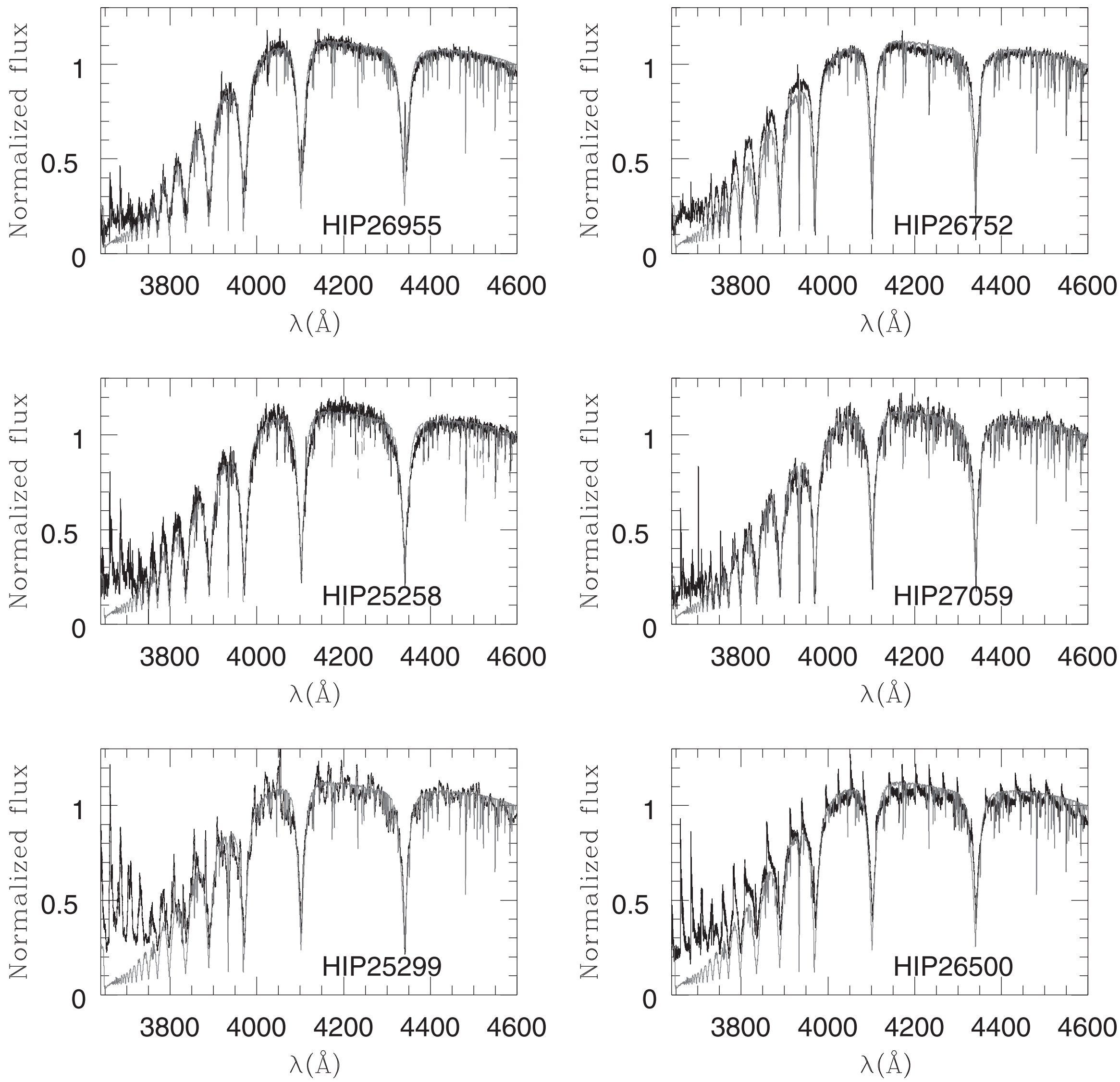

Figure 5. Balmer discontinuity in HAeBes. In each panel, the star is compared with a synthetic template (gray line) of an A0 star from Kurucz (1979). In spite of contamination from line emission, the Balmer excess is evident in all objects.

Large Telescope (VLT; $R = 17{,}000$), using a similar technique for $v \sin i$ determinations. The authors obtain upper limits of $17\,\mathrm{km\,s^{-1}}$ for the majority of the objects with the exception of J05382774-0243009 and J05383431-0235000, whose $v \sin i$ of 23.7 and $31.7\,\mathrm{km\,s^{-1}}$ are in agreement with our measurements. More recently, Kounkel et al. (2018, 2019) analyzed spectroscopic data from APOGEE-2 ($R = 22{,}500$) and reported $v \sin i$ for 45 of our objects. Comparison with our data is indicated by gray squares in the left panel of Figure 3. Our $v \sin i$ values are in agreement with those reported by other authors for velocities above resolution limit of APOGEE-2, i.e., $13\,\mathrm{km\,s^{-1}}$. Concerning HAeBes, we compared our $v \sin i$ values obtained with the CCF method with those obtained from the spectropolarimetric analysis conducted by Alecian et al. (2013). Symbols in black in the right panel of Figure 3 indicate absolute observed differences below $8\,\mathrm{km\,s^{-1}}$.

4. Rotation of TTs and Herbig Ae/Be Stars

In Figure 4 we show the variation of the rotation rate $v \sin i$ with stellar mass obtained through the methodology described in Sections 3.3 and 3.1. We recall that the majority of the objects are reliable members with ages between 3 Myr and 10 Myr, and therefore this distribution well represents the stellar rotation within this age interval. While the age normally adopted for the σ Orionis cluster is 2–4 Myr (e.g., Zapatero Osorio et al. 2002; Peña Ramírez et al. 2012), the ages of Orion OB1a and OB1bc have upper limits of 10 Myr. Nonetheless, high dispersion in the rotation rates for stars younger than 10 Myr is a typical feature among TTs in other young clusters, such as ONC ($\sim$1 Myr; Herbst et al. 2002), Taurus, ρ Oph ($\sim$1–2 Myr; Rebull et al. 2018), and the σ Orionis cluster (Cody & Hillenbrand 2010). In fact, for our sample of TTs we obtain $\langle v \sin i \rangle^{\mathrm{TTs}} = (21 \pm 9)\,\mathrm{km\,s^{-1}}$.

We separate the TTs into accretors and nonaccretors, according to the classification by Hernández et al. (2014) based on the Hα 10% line. We find that 53% correspond to accretors, 27% are nonaccretors, 8% are binary candidates, and 12% lack accretion information. Rotational velocities are slightly larger for nonaccretors ($\langle v \sin i \rangle^{\text{non-acc}} = (24 \pm 9)\,\mathrm{km\,s^{-1}}$) in comparison to accretors ($\langle v \sin i \rangle^{\mathrm{acc}} = (19 \pm 8)\,\mathrm{km\,s^{-1}}$), as expected from MA and confirmed in stellar associations (<10 Myr) by

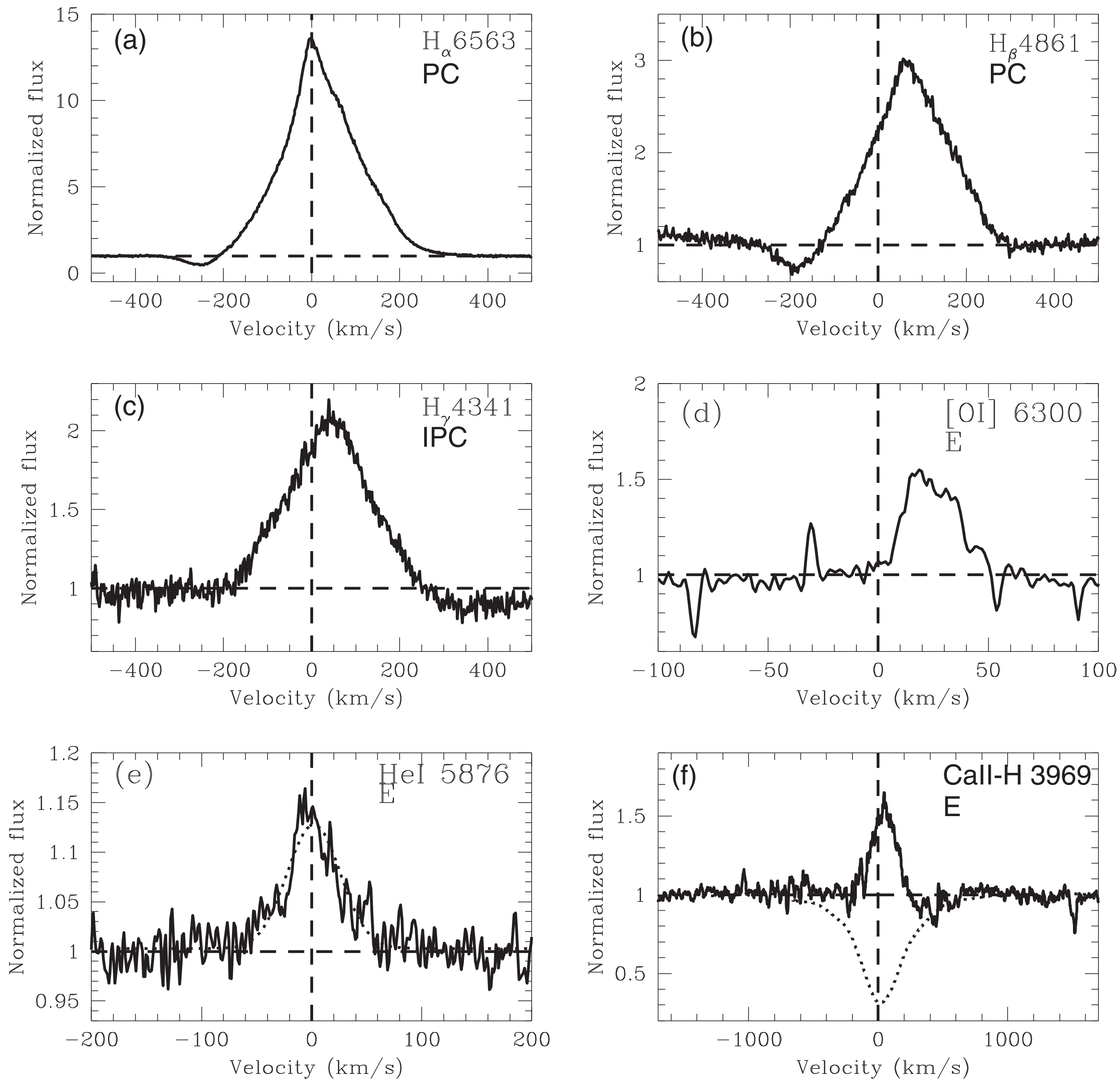

Figure 6. Nonphotospheric line profiles for HIP26955. The continuum, normalized to 1.0, is marked with a horizontal dashed line, while the stellar rest velocity is labeled with a vertical dashed line. Profile classification and spectral line are shown in the upper right of each panel. Panels (a)–(c) correspond to Hα 6563 Å, Hβ 4861 Å, and Hγ 4341 Å, respectively. Panel (d) shows the [O I] 6300.31 Å, and (e) the He I 5876 Å line and a Gaussian fit (dotted). Panel (e) shows the Ca II H 3969 Å line and the photospheric contribution (dotted line). The intensity scales were adjusted so that the continuum for all stars would be the same.

Jayawardhana et al. (2006). Accreting stars rotate, on average, slower than nonaccreting stars. This agrees with the scenario in which the stellar rotation in CTTS is affected by the disk braking phenomena (Bouvier 2013).

Concerning HAeBes, they exhibit rotation rates significantly larger than those in TTs. We report $\langle v \sin i \rangle^{\rm HAeBes} = (115 \pm 9)\,{\rm km\,s^{-1}}$, confirming an increase in $v \sin i$ with stellar mass from TTs to HAeBes by a factor of $\sim$5. We indicated our six objects with squares in Figure 4. While single HAeBes remain roughly constant above $\sim$100 km s^{-1}, the binary system HIP25258 is placed at the bottom of the diagram (open squares). Complementary data of HAeBes of Alecian et al. (2013) and Fairlamb et al. (2015) are also included and shown with filled circles in gray. The binary candidates are indicated by empty circles, with upper limit values indicated by crosses. The two slowest rotators HD190073 and BD051253 are accreting, being active HAeBes. While the former is a $3\,M_\odot$ active HAeBe (Manoj et al. 2006), the latter is a B9 star with an accretion rate of $\log \dot{M}_a = -5.34\,M_\odot\,{\rm yr}^{-1}$ (Fairlamb et al. 2015).

5. The Interplay of Accretion and Winds in HAeBes

In order to confirm whether HAeBes are accreting or not, we searched for excess fluxes in the Balmer discontinuity relative to a stellar template of similar spectral type. Assuming a magnetospheric accretion framework, this excess is related to the accretion rate of protoplanetary disks (e.g., Donehew & Brittain 2011; Rigliaco et al. 2012; Mendigutía et al. 2013). In Figure 5 we show the normalized spectrum of each star to the stellar template in the interval that includes the Balmer jump. Despite the contamination due to emission lines, excess emission in the Balmer discontinuity is observed in all objects. Under the hypothesis of magnetically controlled accretion, this behavior suggests that active accretion processes are present in the HAeBes sample (Cauley & Johns-Krull 2015; Villebrun et al. 2019).

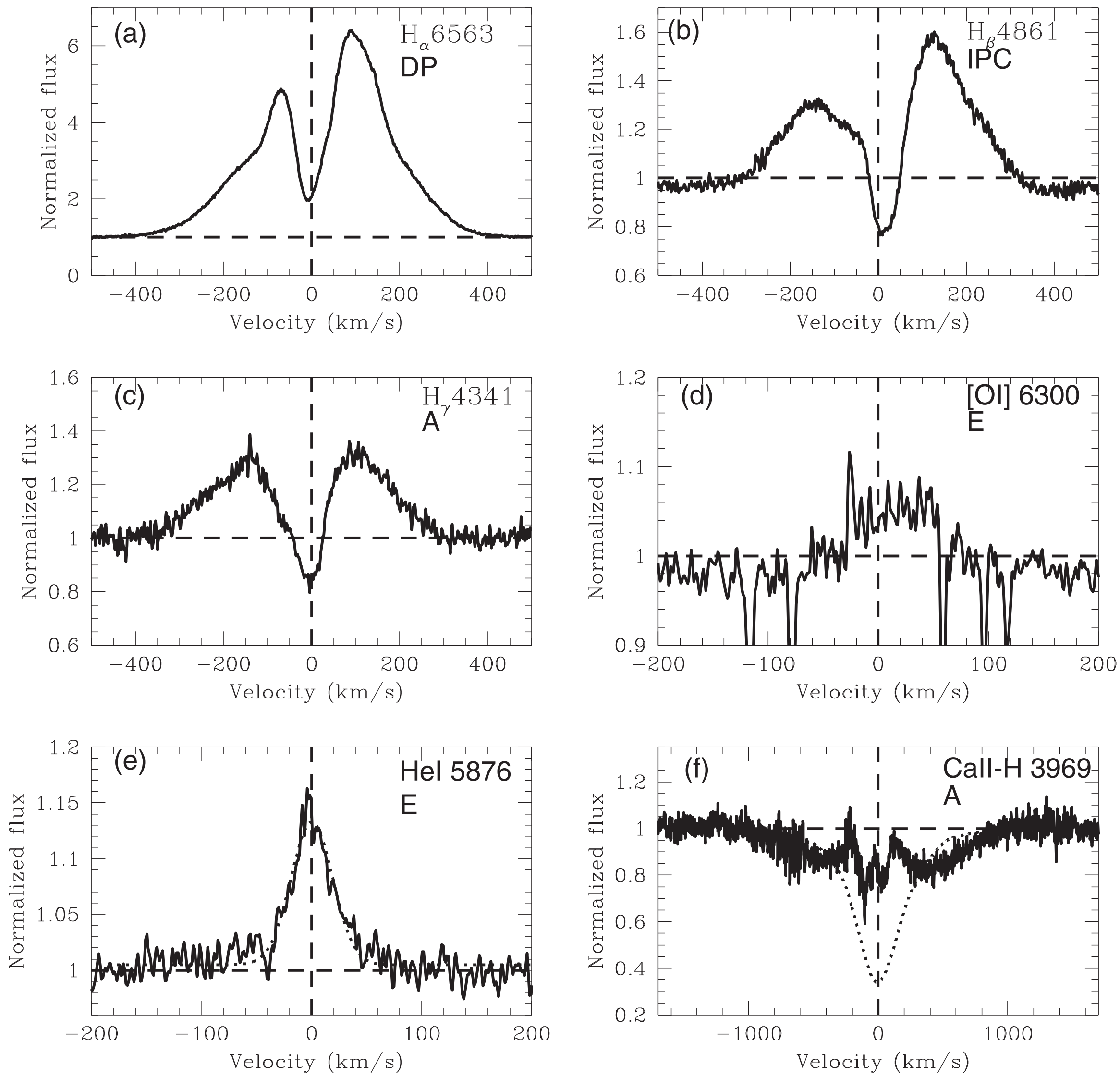

Figure 7. Nonphotospheric line profiles for HIP26752. Symbols are the same as in Figure 6.

Regarding the presence of winds, we examined the morphology of the residual profiles of the FIES spectra searching for mass-loss features in the form of jets and blueshifted forbidden emission lines such as [O I] 6300 Å. Residual profiles were obtained after subtracting the photospheric contribution using the spectrum of a standard star, rotationally broadened to the $v \sin i$ of the target. Panels (a)–(c) of Figures 6–11 show such profiles for the Hα, Hβ, and Hγ Balmer lines. The forbidden line [O I] 6300 Å is shown in panel (d), whereas in panel (e) we show He I 5876 Å, whose physical origin comes from magnetically controlled accretion (Beristain et al. 2001). Finally, the Ca II 3933 Å, recognized as an indicator of chromospheric activity in TTs, is shown in panel (f). We note that all HAeBes exhibit some residual level of emission in this line, relative to the photospheric contribution (dotted lines). These six profiles were classified in groups as follows: Double-peak (DP), Inverse P Cygni (IPC), P Cygni (PC), (E) in emission, (A) in absorption, and (F) flat. It is apparent that Balmer lines show complex profiles with red, central, and blueshifted absorption features that reveal the presence of accretion phenomena of even active chromospheres with inflows and outflows of matter.

In Figure 6 we show line profiles for HIP26955, an object with a clear PC profile in the Balmer lines, with a blueshifted absorption feature dipping below the continuum at $\sim\!-200\,\mathrm{km\,s^{-1}}$ and with the edge extending up to $\sim\!-300\,\mathrm{km\,s^{-1}}$, clear evidence of a stellar wind. This object also shows emission in [O I] 6300 Å with a broad component centered at $\sim\!30\,\mathrm{km\,s^{-1}}$ and extending up to $60\,\mathrm{km\,s^{-1}}$. Although a similar behavior to a smaller degree is exhibited by HIP26752 (Figure 7), the other stars show a very narrow residual emission centered around $-30\,\mathrm{km\,s^{-1}}$ and with a FWHM of $\sim\!5\,\mathrm{km\,s^{-1}}$, which is due to night sky line contamination. The [O I] 6300 Å emission line originates in low-density regions, in the outer parts of stellar winds, and its broadening is associated with the terminal velocity of the stellar wind (Boehm & Catala 1994; Hartigan et al. 1995). In addition to showing forbidden line emission, the HAeBes HIP26955 and HIP26752 show the largest dereddened WISE color indexes $[3.4 - 22]_0\,\mu$m among studied HAeBes, as confirmed by the parameters in Table 4.

In TTs, forbidden line emission correlates with infrared excesses, which is interpreted as winds that are powered in some way by the stellar accretion. High spatial resolution

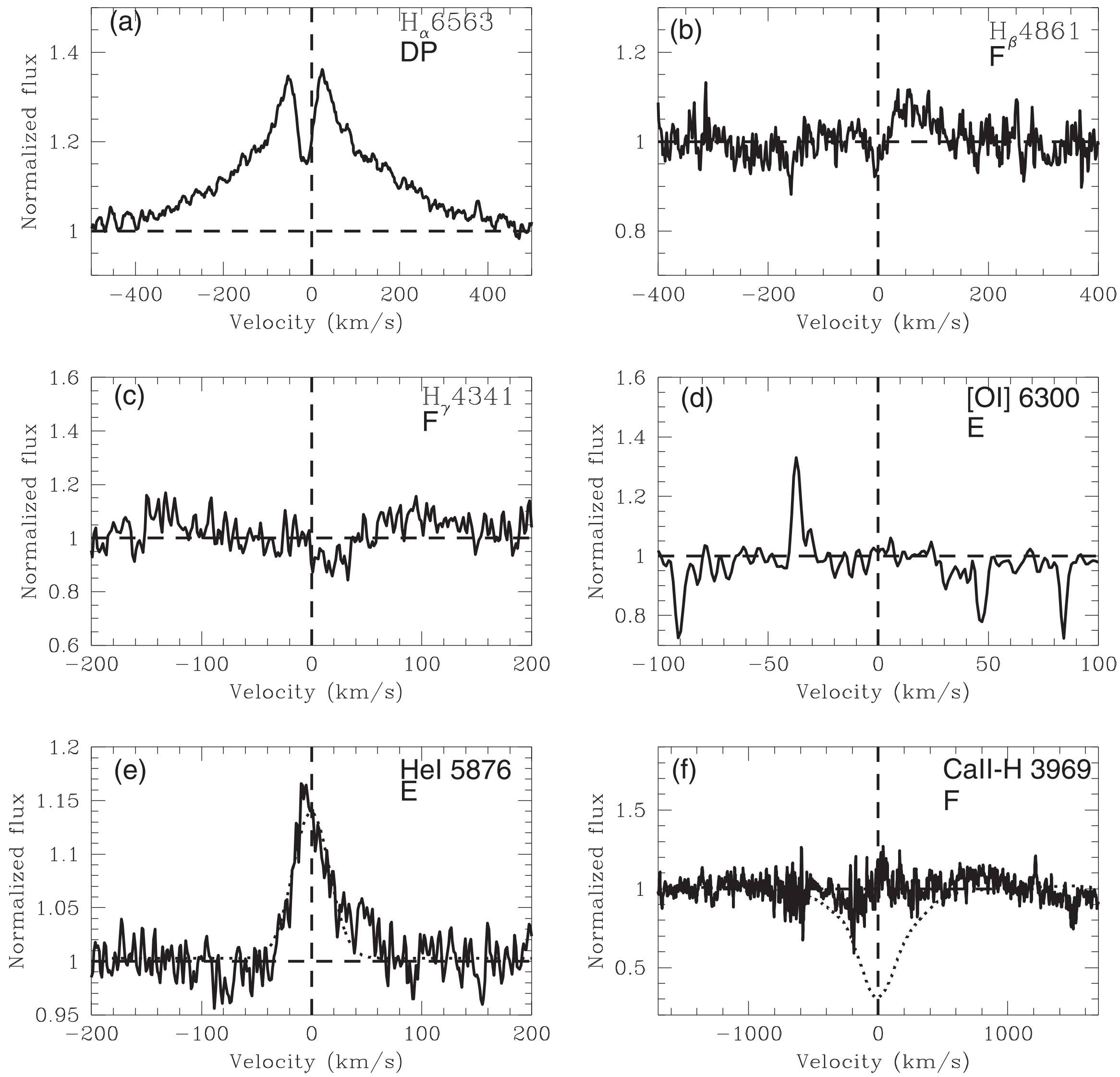

Figure 8. Same as in Figure 6 but for HIP25258.

studies are required for exploring the physics of the wind-launching mechanism in these systems (Hone et al. 2017). Assuming that the stellar accretion powers stellar winds, theoretical models suggest that TTs with mass-loss rates of one tenth of the accretion rate can lose enough angular momentum to keep the stellar rotation locked during the first 3 Myr (Matt & Pudritz 2005; Cranmer 2008). This is supported by the observed morphology of the majority of Balmer emission lines in high spectral resolution, with the presence of simultaneous redshifted and blueshifted absorption features that are interpreted as accretion and winds events, respectively. By contrast, a census of both red- and blueshifted absorption features in large samples of HAeBes confirm lower occurrences in comparison to TTs, as well as differences in the accretion mechanism between Herbig Aes and Bes, suggesting that the innermost environments of HAeBes could not be a scaled version of those of the TTs (Cauley & Johns-Krull 2015). An eventual transition from the magnetospheric accretion/ejection paradigm into other mechanisms such as the boundary layer scenario is thus expected, but more detailed studies are required.

6. Synthetic $v \sin i$–mass Distributions

We derive a set of relations in the $v \sin i$–mass diagram for different disk lifetimes and magnetic field strengths to study general trends between rotation and stellar parameters such as accretion, magnetic field, and the presence of a disk on a spin evolution model. Rather than attempting to explain all phenomena involved in the rotational evolution of TTs and HAeBes, the main goal is to address the question of to what extent the current picture of angular momentum evolution in TTs can be extrapolated toward HAeBes. The source code and all required files are in the public domain.[11]

6.1. Model Assumptions

The model is an extension toward lower and higher masses of the one described by Matt et al. (2012), and it is used to compute the rotational evolution of a solar-mass star, magnetically linked to a surrounding accretion disk during the Hayashi track. We compute the rotational evolution for a

[11] https://github.com/gpinzon/REFUGEE

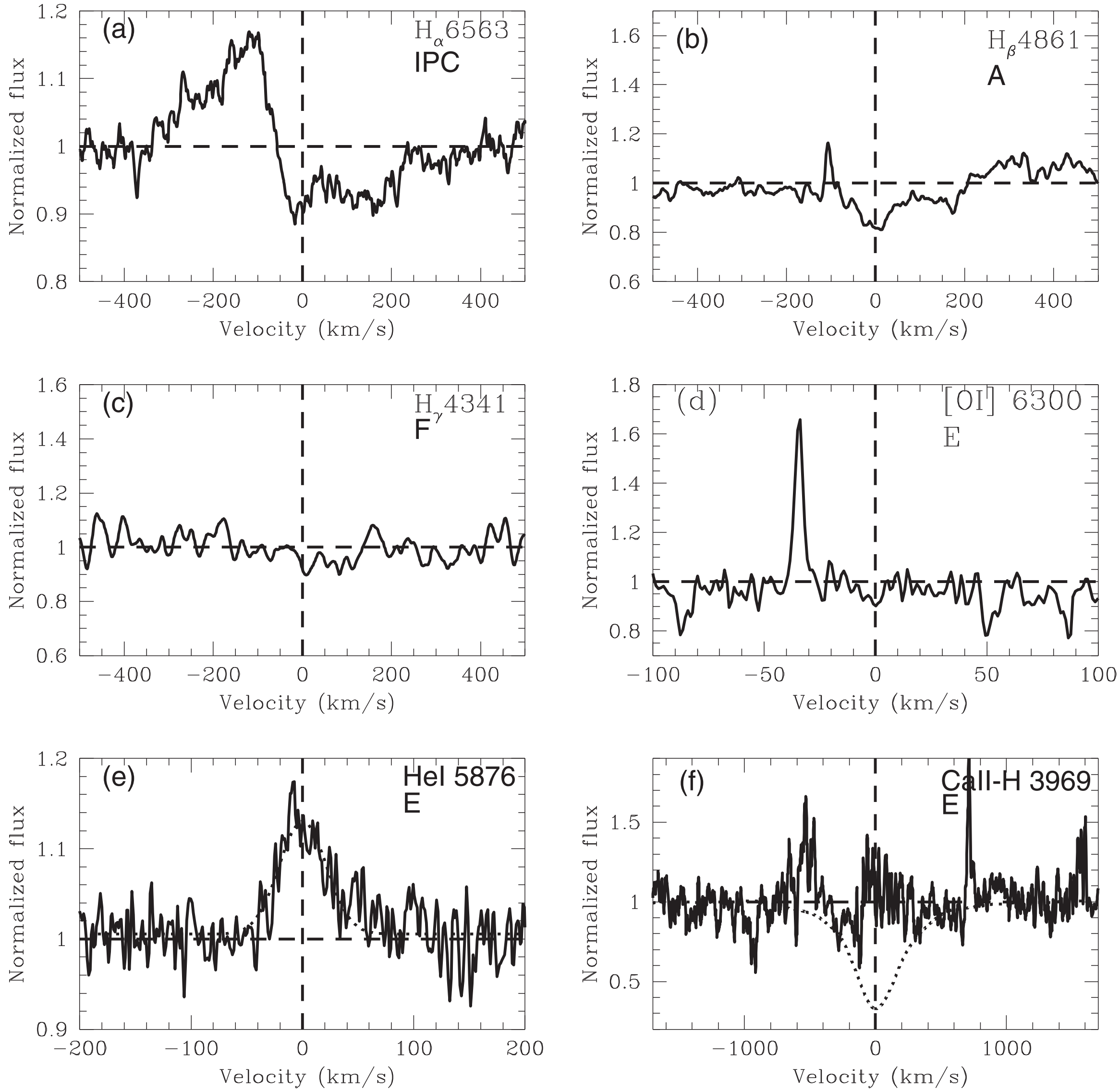

Figure 9. Same as in Figure 6 but for HIP25299.

wide range of masses, from the birth line to the adopted age for σ Orionis (3 Myr). We present calculations of the spin rate of protostellar masses between 0.1 $M_\odot$ and 7 $M_\odot$ at 1, 3, 5, and 10 Myr, considering a range of disk lifetimes between 0.08 Myr and 3.0 Myr and magnetic field strengths in the interval 500–3000 G, representative of TTs and HAeBes. The model relies on the following assumptions:

Solid body rotation: To model the rotational evolution, we assume uniform internal rotation, although the stellar interior is described by nonrotating evolutionary stellar models. The internal structure of stars is obtained from the grid of 27 PMS mass tracks of Siess et al. (2000) for solar metallicity ($Z = 0.02$) spanning over 0.1–7.0 $M_\odot$. We find it reasonable to assume that TTs are well described by the interval $0.1 \leqslant M_* \leqslant 1.5\,M_\odot$, whereas HAeBes fit the condition $M_* > 1.5\,M_\odot$ (Hillenbrand et al. 1992).

Disk-locking: This effect arises from the magnetic interaction between the star and the surrounding gaseous disk. This stage lasts a few Myr (Bouvier 2013) and depends on both the magnetic coupling strength to the disk and the opening of magnetic field lines due to differential rotation (Uzdensky et al. 2002). We used the same assumptions described in Matt & Pudritz (2005) and Matt et al. (2010) for the calculation of this magnetic torque that are summarized as follows: (1) a critical twisting $\gamma_c = 1$, which represents comparable azimuthal and vertical magnetic field components within the disk in order for the dipolar field lines to remain closed, and (2) a magnetic diffusivity parameter $\beta = 10^{-2}$, which describes strong coupling between the star and disk (Rosen et al. 2012). The disk-locking durability is given by the disk lifetime τ_D, which is a free parameter of the model. We consider the following cases: $\tau_D = 0.08$, 0.5, 0.7, 1.0, 2.0, and 3.0 Myr.

Stellar winds: In TTs, powerful winds arising from open field regions, i.e., accretion powered stellar winds (APSWs) have been shown to be the primary agent or one of the most important agents for removing angular momentum from the star (Hartmann et al. 1982; Romanova et al. 2005; Matt et al. 2012). It is assumed that in these stars a fraction χ of the energy released during the accretion process is dissipated close to the star surface and transferred to the stellar wind. The stellar wind torque T_w in the APSWs scenario is given by:

$$T_w = -\dot{M}_w \Omega_* r_{\rm A}^2, \tag{1}$$

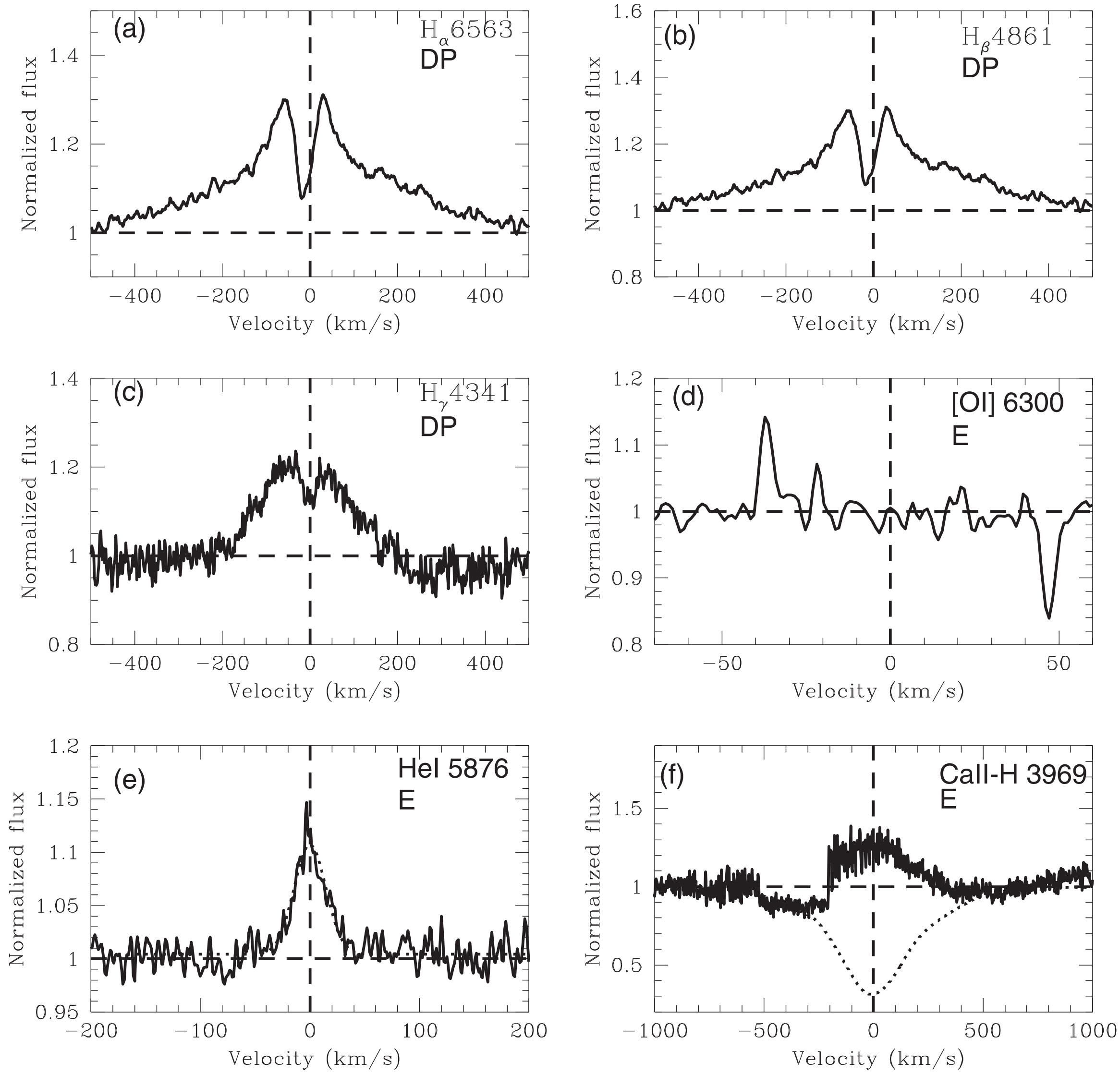

Figure 10. Same as in Figure 6 but for HIP26500.

where $\dot{M}_w = \chi \dot{M}_a$ is the mass-loss rate in the wind, $\dot{M}_a$ is the stellar accretion rate, $\Omega_* = v_* R_*$ is the angular velocity of the star, and r_A is the location where the wind speed equals that of magnetic Alfvén waves. These radii were computed based on solutions for two-dimensional axisymmetric solar-like stellar winds (Matt & Pudritz 2008). The mass-loss-weighted average of the Alfvén radius in the multidimensional flow is thus computed through the relation:

$$\frac{r_A}{R_*} = K\left(\frac{B_*^2 R_*^2}{\dot{M}_w v_{esc}}\right)^m. \quad (2)$$

Here, B_* is the stellar magnetic field, R_* the radius of the star, $\dot{M}_w$ the wind mass-loss rate, and v_{esc} the escape velocity. In concordance with the main purpose, which is an extension of the model toward higher masses maintaining same physics, we fixed K and m in all our simulations. Following Matt & Pudritz (2008) and Matt et al. (2012), we adopted $K = 2.11$ and $m = 0.223$, which are in agreement with recent 2.5D magnetohydrodynamic simulations of Pantolmos et al. (2020). Concerning the wind mass loss, it is computed at any instant of time through $\dot{M}_w = 0.1 \times \dot{M}_a$, i.e., $\chi = 0.1$ (Hartmann & Stauffer 1989; Matt & Pudritz 2005; Cabrit 2007; Ahuir et al. 2020). Finally, we recall that T_w is null for $t > \tau_D$.

Changes in the accretion rate: We assume that accretion depends on both mass and time as follows:

$$\dot{M}_a(M_*, t) = \dot{M}_{a,0}(M_*) e^{-t/\tau_a}, \quad (3)$$

where $\dot{M}_{a,0}$ is the accretion rate at the birthline and τ_a is the characteristic timescale for the temporal decay. The decay of accretion cannot be explained entirely through an empirical relationship with age; however, observations in open clusters confirm a decay as t^{-k} with k between -1.6 and -1.2 (Hartmann et al. 1998; Sicilia-Aguilar et al. 2010; Manzo-Martínez et al. 2020). For the exponential decay in Equation (3), we find it plausible to adopt $\tau_a = 8$ Myr in all simulations, which is an intermediate value between the average disk lifetime of 3–5 Myr used by Gallet & Bouvier (2015) and maximum lifetimes of 10–20 Myr measured by Bell et al. (2013).

The accretion rates for TTs and HAeBes, determined from spectroscopic observations, correlate with the mass of the star through a power law $\dot{M}_a \propto M_*^\alpha$, with α between 1.5 and 3.1

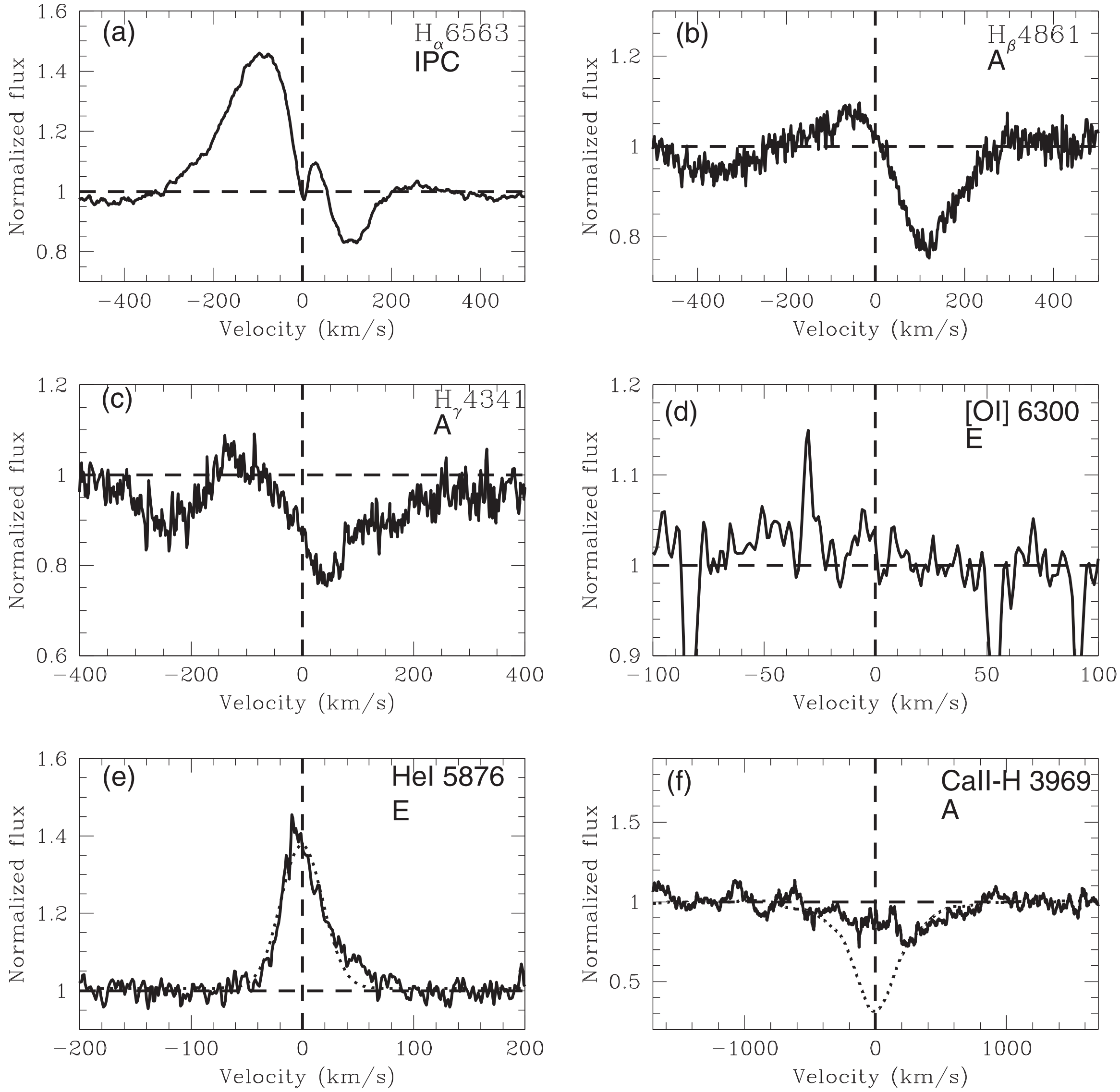

Figure 11. Same as in Figure 6 but for HIP27059.

(Muzerolle et al. 2004; Manara et al. 2015). Under the assumption that this correlation is maintained at the birthline as well, we are able to compute initial accretion rates for a wide range of masses. We prepared a compilation of accretion rates at 3 Myr as shown in Figure 12. For TTs we used members studied by Rigliaco et al. (2012) and Maucó et al. (2016), whereas for HAeBes we used data from Alecian et al. (2013) and Fairlamb et al. (2015). By considering the sample as a whole, the best fit is reached with $\alpha = (2.51 \pm 0.20)$, in agreement with the exponents obtained in other star-forming regions such as Taurus (Calvet et al. 2004) and Ophiuchus (Natta et al. 2006), although a more steep correlation ($4.6 < \alpha < 5.2$) between accretion rates has been reported in HAeBes (Mendigutía et al. 2012), with notable differences between HAes and HBes. The scatter in Figure 12 remains constant at about two orders of magnitude throughout and is explained by variability, errors in mass estimation from stellar models, and bias attributed to sample selection (Hartmann et al. 2016).

Magnetic field strength: It is assumed that the star has a uniform co-rotating dipolar magnetic field with strength B_* anchored to its surface. This stellar field connects to an extended disk region, reaching beyond the disk co-rotation radius depending of its strength, which, in turn, depends on the spectral type. For TTs with masses above the convective limit ($M_* \gtrsim 0.3\,M_\odot$), the assumption that magnetic field forms via a solar-type dynamo $\alpha - \Omega$ is consistent with the observed strengths in the range $1 < B_* < 5$ kG (Vidotto et al. 2014). In addition, magnetic fluxes of stars with masses between $0.3\,M_\odot$ and $2.0\,M_\odot$, scale up with the rotation rate until the saturation that is supported by the stellar dynamo theory. In fully convective stars ($M_* \lesssim 0.3\,M_\odot$), the absence of an interface dividing radiation from convection prevents the generation of magnetic fields via a solar-type dynamo. However, theoretical models suggest that small-scale fields may be amplified and transformed into nonaxisymmetric large-scale fields under the action of differential rotation (Dobler et al. 2006; Browning 2008). Very low-mass TTs ($M_* \lesssim 0.2\,M_\odot$) display a variety of strengths and topologies being the large-scale fields that are predominantly poloidal and axisymmetric, with strengths on the order of a few kilo-Gauss, as confirmed through the analysis of their highly polarized rotationally modulated radio emission (Berger 2006).

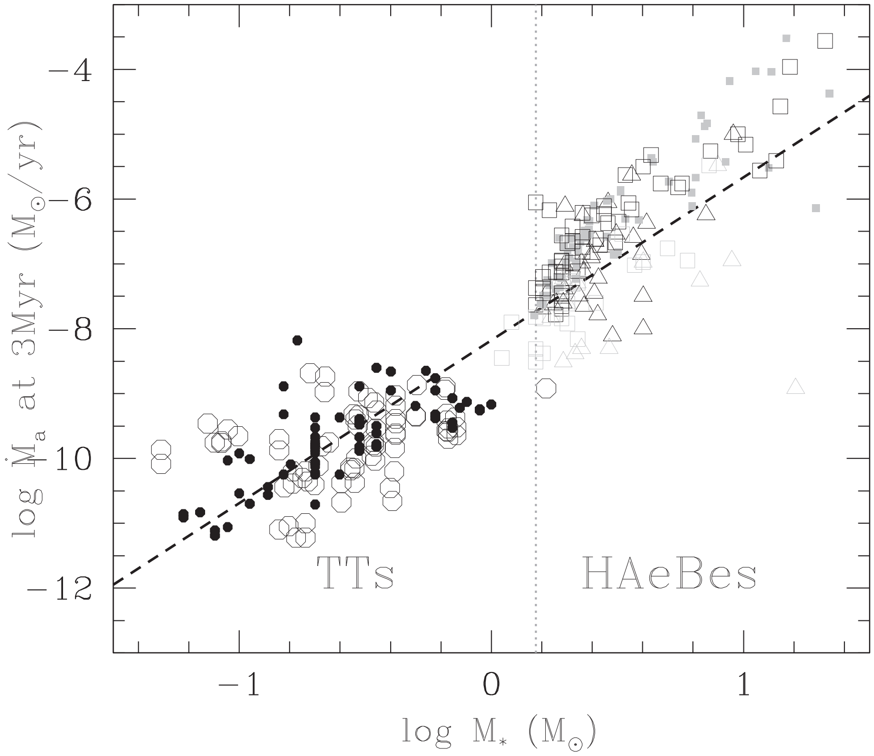

Figure 12. Compilation of stellar accretion at 3 Myr: TTs from Rigliaco et al. (2012; filled circles) and Maucó et al. (2016; open circles). HAeBes from Fairlamb et al. (2015; open squares in black), Alecian et al. (2013; open triangles in black). The vertical line represents the limit between TTs and HAeBes, whereas the straight line corresponds to the best fit with $\alpha = (2.51 \pm 0.2)$. This exponent is in agreement with that obtained with the data reported in the recent study by Wichittanakom et al. (2020; filled squares in gray). We used this match in order to obtain the accretion rates at the birthline (see the text).

That said, magnetic fields in HAeBes are scarce, with fewer than 10% of large samples hosting large-scale dipolar fields stronger than 0.3 kG (Wade et al. 2007; Alecian et al. 2013). We note that this statistic is based on measurements with too large uncertainties that prevent detections on the order of a few tens to a few hundred Gauss. The study by Hubrig et al. (2015) suggests that the low detection rate of magnetic fields in HAeBes can be plausibly explained by the limited sensitivity of the published measurements and by the weakness of the magnetic fields in these stars. Regardless of these factors, the large-scale fields among the few magnetic HAeBes have similar strengths to those displayed by the slowly rotating Ap/Bp stars on the main sequence (Kochukhov & Bagnulo 2006; Aurière et al. 2007). The presence of magnetic fields in HAeBes and their disappearance at evolutionary stages closer to the main sequence (see Hubrig et al. 2009a, 2015) indicate that these fields are probably remnants of the magnetic fields generated by dynamos during the convective phases at early PMS stages. In this context, HAeBes with strong kilo-Gauss fields can be considered progenitors of Ap/Bp stars (Ferrario et al. 2009). For this work, we find it reasonable to assume that fields in HAeBes are already present at the birthline and survive the pre-main sequence all along. The rotational models presented here were computed separately for the four constant strength values of $B_* = 0.5$, 1.0, 2.0, and 3.0 kG.

6.2. Numerical Method

The evolution of angular velocity Ω_* is computed as follows:

$$\frac{d\Omega_*}{dt} = \frac{T_*}{I_*} - \Omega_* \left[\frac{\dot{M}_a}{M_*}(1 - \chi) + \frac{2}{R_*}\frac{dR_*}{dt} \right], \qquad (4)$$

where I_* is the stellar moment of inertia of the star, $\chi = 0.1$ (Cabrit 2007; Matt et al. 2012) is the fraction of the accretion that goes into the wind, and T_* is the net torque. We recall that T_* has three contributions coming from accretion, stellar winds, and star–disk interaction. This total torque is artificially set to zero for $t \geqslant \tau_D$, where τ_D is the gas-disk lifetime. We used a family of disk life spans ranging from long-lived disks ($\tau_D = 3$ Myr) up to diskless stars ($\tau_D = 0.08$ Myr).

6.2.1. Initial Conditions

In the absence of information about initial angular velocity, we fixed it at the beginning of the PMS to one-third of the break-up limit or critic velocity v_c in all cases. This assumption is supported by the fact that under sufficiently high field strengths and accretion rates, the stellar rotation quickly reaches an equilibrium in which Ω_* is independent of initial rotation (Collier Cameron et al. 1995). Regarding initial stellar mass and radius, they were obtained from interpolation based on the evolutionary models of Siess et al. (2000).

The initial accretion rate values were computed assuming $\dot{M}_a = M_*^{\alpha}$ with $\alpha = (2.51 \pm 0.20)$. We integrated Equation (3) inward in time in order to get $\dot{M}_{a,0}$ for each mass. This results in initial accretion rates in TTs of $\dot{M}_a = 5 \times 10^{-9} M_\odot$ yr^{-1} that lead to initial disk masses on the order of $M_D = 0.03\, M_\odot$, which is compatible with disk masses of $\sim 0.02\, M_\odot$ estimated from cold dust emission (Hartmann et al. 1998). For HAeBes we obtain $\dot{M}_a = 5 \times 10^{-7} M_\odot$ yr^{-1} and thus initial disk masses with a median of $M_D = 0.65\, M_\odot$, consistent with values reported by Mendigutía et al. (2012). Despite being low, the derived values reflect the observed trend with mass displaying

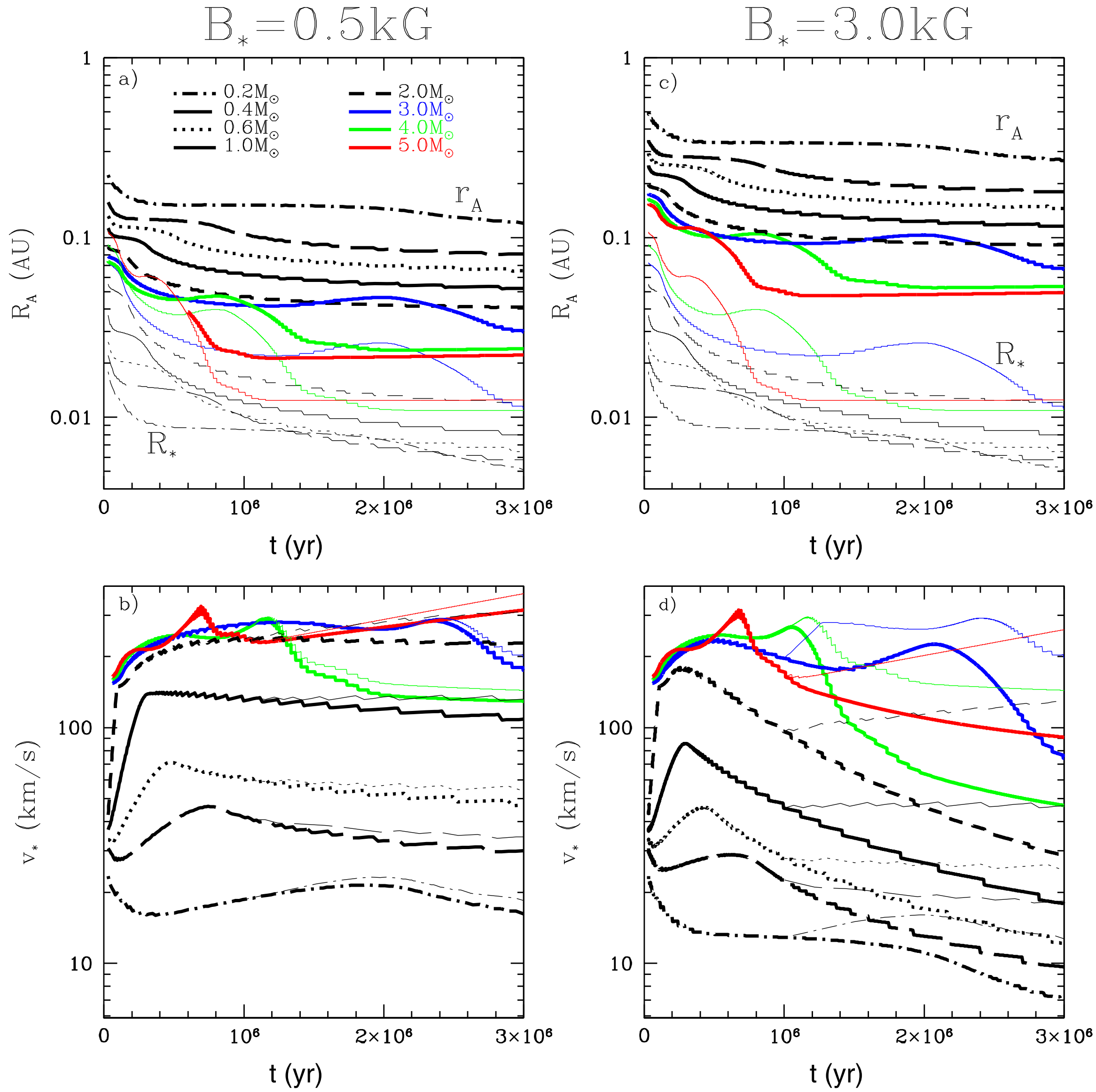

Figure 13. Time evolution of r_A and v_* for two magnetic field strengths. Panels (a) and (b) show the Alfvén radii in astronomical units and stellar rotational velocities in km s^{-1}, respectively, for $B_=$ 0.5 kG. Panels (c) and (d) were obtained using $B_* = 3.0$ kG. Thick lines of a given color or type represent eight rotational models of protostars with long-lived disks ($\tau_D = 3$ Myr) and with masses between 0.2 and 5.0 $M_\odot$. Thin lines in panels (b) and (d) represent the rotational evolution for $\tau_D = 1$ Myr, whereas in panels (a) and (b) thin lines follow the stellar radius evolution as given by Siess et al. (2000).

high dispersion and therefore they might be considered just representative values.

We integrated Equations (3) and (4) using the fourth-order Runge–Kutta scheme of Press et al. (2007) with adaptive step size. At each time step, we calculated the next one by requiring that none of the variables change by more than 1% per step. This scheme required just a few hundred time steps to complete the computation from the birthline $\tau_0 = 0.08$ Myr up to 1, 3, 5, or 10 Myr. In the computation, the I_* and R_* values from Siess et al. (2000) models were interpolated using a third-degree polynomial.

7. Results

We first consider two rotational histories during the first 3 Myr after the birthline, with the same initial conditions and disk lifetime ($\tau_D = 3.0$ Myr), but varying the magnetic field strength. Figure 13 shows the evolution of the stellar radius R_*, Alfvén radius $r_{,A}$ and equatorial velocity v_* for $B_* = 0.5$ kG (panels (a) and (b)) and $B_* = 3.0$ (panels (c) and (d)). Models for distinct masses are indicated with thick lines of different types and colors. HAeBes are represented by lines in blue, green, and red, whereas TTs are shown by lines in black with distinct line types. We recall that rotation in TTs and very likely in HAeBes tends toward a rotational equilibrium in which the total torque on the star would be zero. From Figure 13 it is clear that in both groups of stars, the spin rate increases substantially with time at the beginning of the simulations, due to accretion and the rapid contraction of the star, both adding angular momentum. We note that the Alfvén radius in the stellar wind for the model of 5 $M_\odot$ and for the case of low field strength coincides with the stellar radius during the first $\sim 6 \times 10^5$ yr. Considering that this model reaches the main sequence at 3 Myr, that time represents 20% of its PMS lifetime. That said, field strengths in the range of kilo-Gauss enable efficient angular momentum loss since the beginning of evolution. From Figure 13 it is evident that higher fields

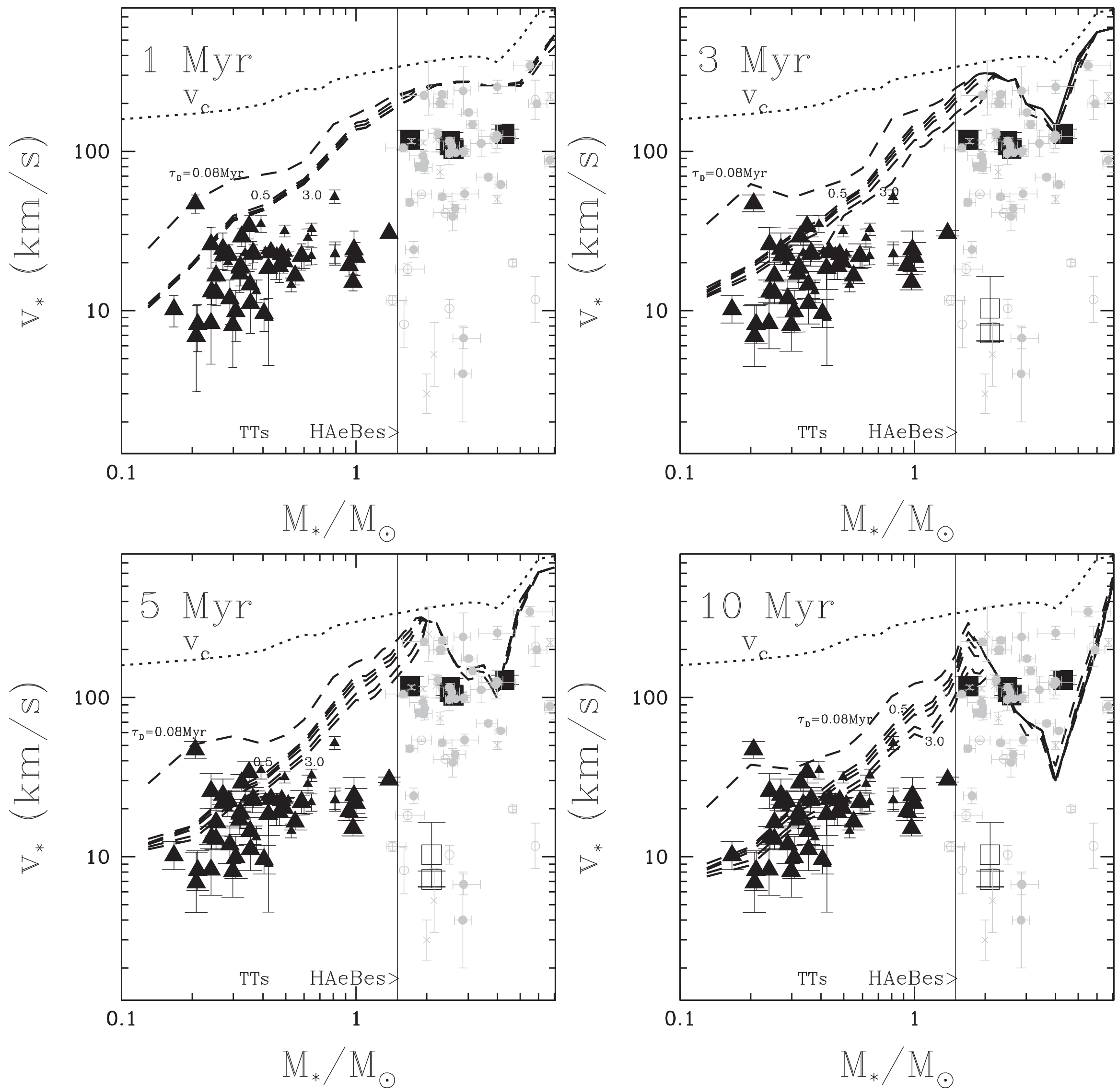

Figure 14. Snapshots of the stellar rotation against mass at 1, 3, 5, and 10 Myr for $B_* = 0.5$ kG. The equatorial rotational velocities (v_*) are indicated with dashed lines for the six gas-disk lifetimes $\tau_D = 0.08$, 0.5, 0.7,1.0, 2.0, and 3.0 Myr. The break-up limit v_c at the birthline is plotted with a dotted curve. Our $v \sin i$ measurements are indicated with filled triangles in black (TTs) and filled squares in black (HAeBes). Accretors among TTs are indicated with bigger triangles. The complementary samples of Cody & Hillenbrand (2010) and Alecian et al. (2013) are shown in gray. Binaries are indicated with empty circles, while limit values of $v \sin i$ are diagonal crosses. The vertical dashed line marks the arrival to the main sequence, while the horizontal dotted line corresponds to the median value of the rotational velocities of our HAeBes sample.

produce larger r_A and thus a more effective spin-down torque. We find that for the case of 3 kG, HAeBes undergo a spin down by a factor of almost 3 at the end of the simulations.

The expected stellar spin up resulting from an early absence of a disk ($\tau_D = 1$ Myr) is indicated in Figures 13(b) and (d) with thin lines of similar types and colors. Results are in line with a disk-locking scenario in which, once the gas within the disk dissipates due to stellar accretion and disk photoevaporation phenomena, the contraction proceeds, rapidly increasing the stellar rotation (Sicilia-Aguilar et al. 2010; Bouvier 2013). For both TTs and HAeBes, the separation between rotational tracks computed with $\tau_D = 1$ and 3 Myr results is significantly larger for $B_* = 3$ kG, as illustrated in panels (c) and (d).

As equilibrium spin rate is reached by 3 Myr, roughly the mean age of our sample, we computed a set of synthetic mass–$v \sin i$ relations at fixed ages of 1, 3, 5, and 10 Myr. These time snapshots of stellar rotation were calculated for distinct stellar magnetic field strengths B_* and disk lifetimes τ_D as shown in Figures 14–17. We consider six disk lifetimes ranging from 0.08 Myr to 3.0 Myr and four magnetic field strengths of 0.5, 1, 2, and 3 kG. For each pair (τ_D, B_*) we obtain a rotational track indicated with a dashed curve in the mass–$v \sin i$ diagrams. In all cases, tracks lie below the critical velocity v_c (dotted line) with a pronounced dip at 4.0 $M_\odot$, a consequence of the shell burning of deuterium that swells up the star significantly and thus induces a sudden spin down (Hosokawa & Omukai 2009). We divide the evolution in this mass region into a swelling phase for $2\,M_\odot \lesssim M_* \lesssim 4\ M_\odot$, followed by a phase of rapid gravitational contraction for $M_* \gtrsim 4\,M_\odot$. From Figures 14 and 15 it is clear that field strengths of order one hundred Gauss are unable to predict the existence of slowly rotating TTs and HAeBes. The poor impact of distinct τ_D's, especially at 1 Myr, is also clear. It can be seen that a large number of TTs with active accretion are located in a region not covered by the

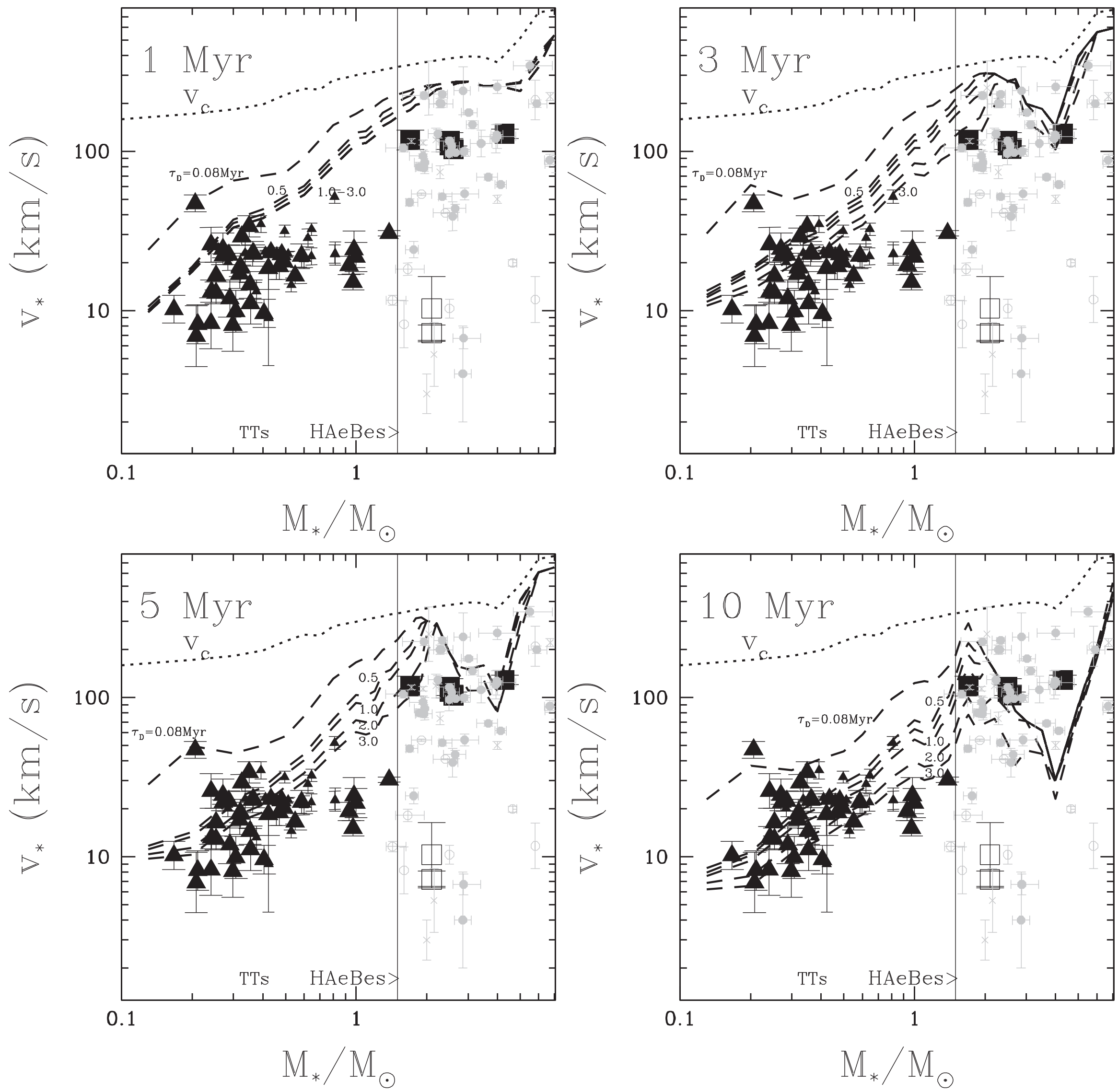

Figure 15. Results for $B_* = 1$ kG in the same format as in Figure 14. The spin down is slightly larger and changes in velocity for distinct τ_D's are noted, especially in the TTs zone.

models. In Figures 16 and 17 higher field strengths lead to larger splitting of tracks corresponding to distinct disk lifetimes, confirming that the presence of a disk is compatible with fields strengths of the order of a kilo-Gauss, as expected for TTs (Muzerolle et al. 2004; Gallet & Bouvier 2015). In particular the set of rotational tracks associated with the pairs (10 Myr, 2 kG) and ($\tau_D \geqslant 3$ Myr, 3 kG) match well the range of velocities and masses covered by our sample.

7.1. Angular Momentum Evolution in Herbig Ae/Be Stars

In order to quantify differences between the data and the models, we used the specific angular momenta $(J \sin i)/M_*$ instead of $v \sin i$. In this section we first describe the systematic trends with mass and thus compare with specific angular momenta obtained using our rotational model. Figure 18 represents the angular momenta for all TTs (triangles) and HAeBes (rectangles) obtained through $(J \sin i)/M_* = k^2 R_* (v \sin i)$, where the gyration radii are given by Siess et al. (2000). We see a gradual increase of angular momenta with mass in the interval 0.1–4.0 $M_\odot$, with a mean value of 5×10^{17} cm^2 s^{-1} for HAeBes. As a reference, the dashed gray line represents the empirical relationship $\langle J/M_* \rangle \propto M_*^{1.02}$ (Kawaler 1987), valid for mature main-sequence stars and constructed assuming stars rotate as solid bodies to a fixed fraction of their critic value. While projection effects contribute less than 15% to the scatter (Wolff et al. 2004), changes in the magnetic fields and fast disk dissipation could play an important role.

In addition, in Figure 18, the angular momentum tracks were computed for the case $\tau_D = 3.0$ Myr with the exception of the dotted line, which represents diskless stars. Although the dispersion is large, the data scatter is fitted reasonably well by the tracks corresponding to $B_* = 2.0$ kG and 3.0 kG. Table 5 shows the Kolmogorov–Smirnov (KS) statistic and p-value or probability that observed and expected values are drawn from the same distribution. For TTs with $B_* \leqslant 1$ kG we can reject the null hypothesis, since the p-value is negligible. However, for 2 kG and 3 kG, the hypothesis cannot be rejected because p-values are 71% and 10%, respectively. The best match of TTs with the model occurs for $B_* = 2.0$ kG, which has the smallest KS statistic and the largest p-value. Concerning HAeBes, the highest p-value of 63% is obtained for $B_* = 2.0$ kG, as well.

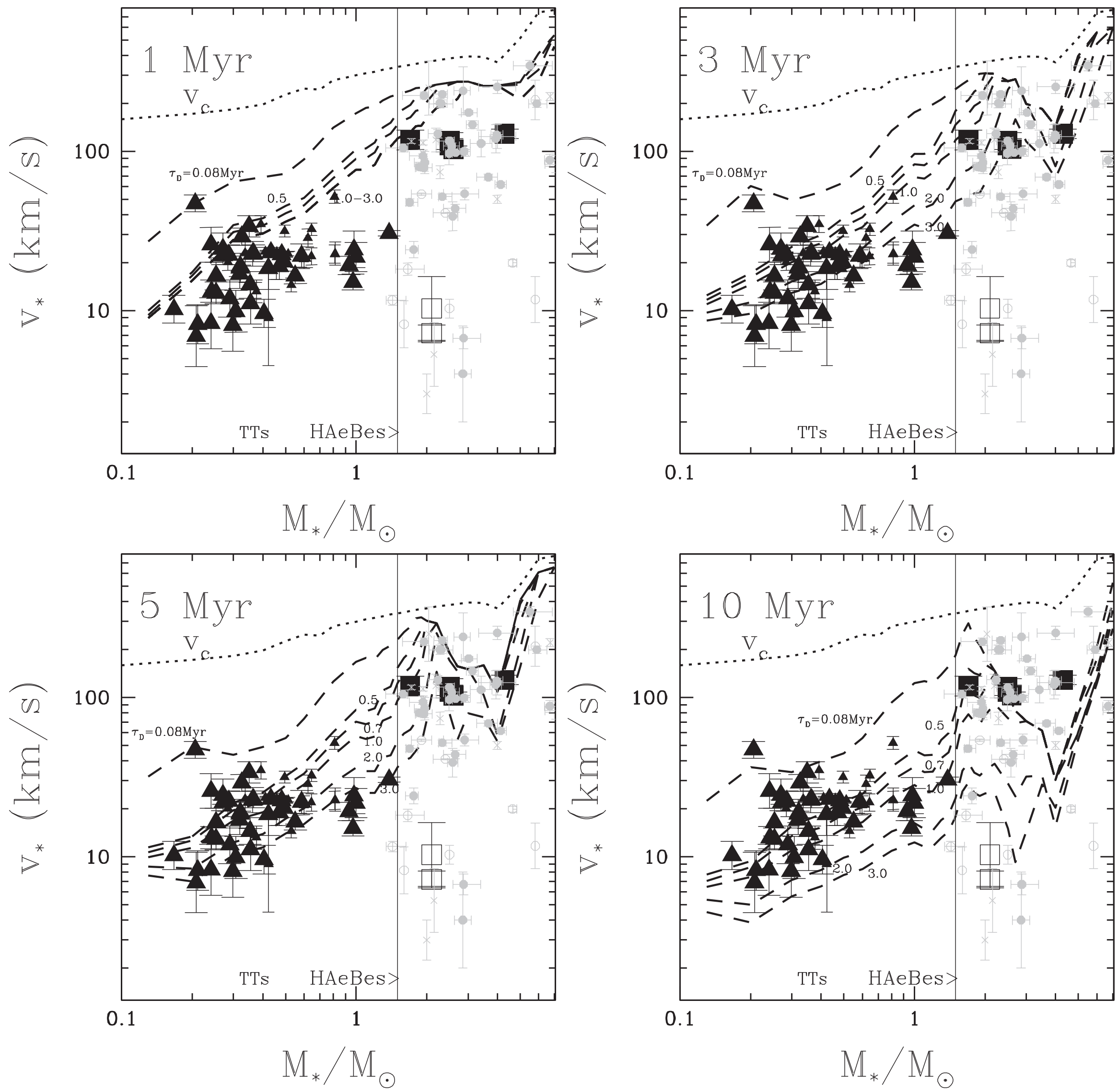

Figure 16. Results for $B_* = 2$ kG in the same format as in Figure 14. Spin down has progressively increased, reaching values of 10% at 10 Myr. Although the best match with the data is obtained for this age, HAeBes remain unmatched.

The other strengths lead to *p*-values below 24%, and therefore we can reject the null hypothesis for them. For the particular case of $B_* = 2.0$ kG, indicated with a thick dotted–dashed line, we compute their separation from the main sequence and find that, on average, TTs ($<1.5\,M_\odot$) have larger specific angular momenta by a factor of 5/2. This dramatic increase in the angular momentum between $2\,M_\odot$ and $3\,M_\odot$ is due to structural changes related to both deuterium burning and the star reaching the main sequence. In this region, $\langle J/M \rangle$ is larger than in the main sequence by a factor of 3.2.

Fields strengths of a few kilo-Gauss are in line with measurements of circular polarization of Ap/Bp main-sequence stars (Alecian et al. 2013). In Figure 18 we indicate with pentagons the specific angular momentum computed for the sample of 23 Ap/Bp stars studied by Aurière et al. (2007). Masses and ages were computed using evolutionary MIST models by Dotter (2016), via effective temperatures and luminosities reported by the authors and the methodology described in Section 3.1. They find longitudinal components larger than a few tens of Gauss and use this information to infer the dipolar component of the field. The size of the pentagons in Figure 18 is proportional to this dipolar component, whose minimum and maximum values are 0.10 kG and 8.9 kG, respectively. The authors report a plateau at about 1 kG, falling off to larger and smaller fields. Two main groups in the form of a bimodality are observed: a slow group of Ap/Bp with roughly high dipoles and $\langle J \sin i/M_* \rangle = 6.3 \times 10^{15}$ cm^2 s^{-1}, and a second group with a weak dipolar component with larger J/M's by a factor of $\sim$6.

How to connect these results with angular momentum in HAeBes is not clear yet, in particular because Ap/Bp stars are found mostly in clusters older than 10^8 yr (Abt 1979). Several works have pointed out that these stars do not experience substantial magnetic braking during their life on the main sequence (North 1998; Kochukhov & Bagnulo 2006). However, this conclusion depends strongly on the origin and evolution of magnetic fields, a subject that still is under debate. Basically, there are three scenarios. (1) The magnetic field appears once the star has spent a considerable fraction of its existence on the main sequence (Hubrig et al. 2000). (2)

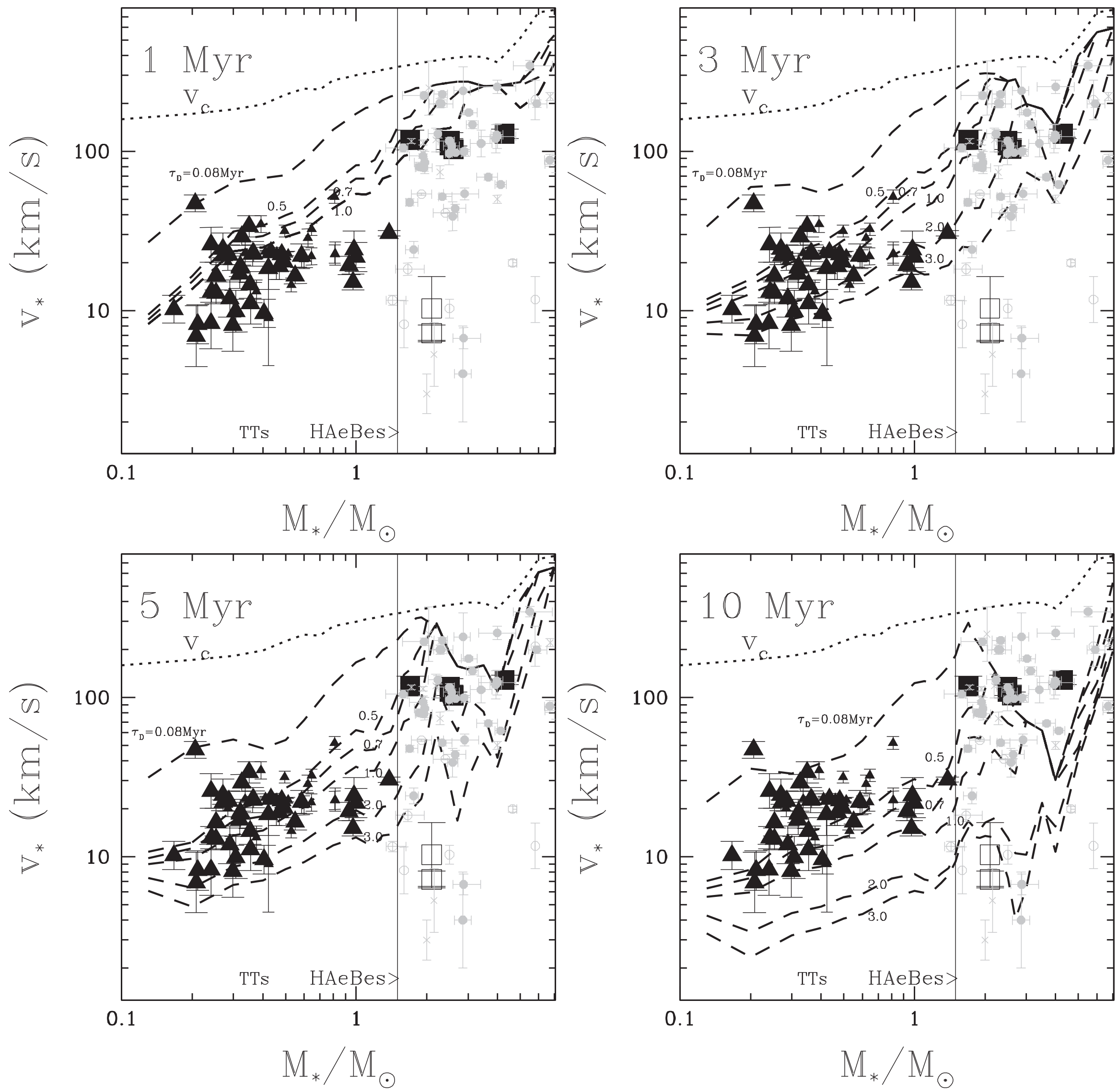

Figure 17. Results for $B_* = 3$ kG in the same format as in Figure 14.

Magnetic fields in Ap/Bp stars are present at the birthline already (Moss 1989; Kochukhov & Bagnulo 2006). Studies based on the analysis of chemical anomalies suggest that magnetic fields are shaped during the first Myr and do not undergo considerable changes after (Gomez et al. 1998; Pöhnl et al. 2005; Wade et al. 2007). This is in agreement with theoretical predictions for the ohmic decay of the field inside the stellar interior, which is nonnegligible, only in scales of Gyr, much longer than the main-sequence lifetime for Ap/Bp stars (Moss 1984). (3) The magnetic field appears during the PMS stage, as a consequence of a merging between two low-mass stars (Ferrario et al. 2009). This merging event occurs when one of the two objects, at least, has arrived at the end of its Henvey track in the H–R diagram (Iben 1965). The resultant merged object has stronger differential rotation and therefore a large-scale dynamo field.

In Figure 18 we have included complementary data of HAeBes from the compilation by Alecian et al. (2013). Single stars are indicated with rectangles in gray, whereas binaries are indicated with open symbols. The two slowly rotating objects located in the Ap/Bp region are HD190073 (spT A1) and BD-06 1253 (B9). The former has marginal reported detections of a magnetic field, although it displays λ Boo–like chemical peculiarities (Castelli et al. 2020). These stars' low rotation rate is explained due to inclination effects (Järvinen et al. 2019). The star BD-06 1253 exhibits weak Ap/Bp peculiarities on its surface composition. Reipurth et al. (2013) have proposed that this star belongs to a quadruple system formed by a Herbig Be, which in turns is a spectroscopic binary (Leinert et al. 1997). In addition, BD-06 1253 is a possible source of outflows observed in radio frequencies (Rodríguez et al. 2016). However, magnetic field measurements of this object are uncertain because no periodicity was found in the behavior of the most prominent emission lines (Alecian et al. 2009). Therefore, it is quite possible that the chemically peculiar component with the detected dipolar magnetic field is not an HAeBe, but already a star at an advanced age, probably on the main sequence. That said, the Herbig Be status of the primary component is merely based on the appearance of emission in the abovementioned lines belonging to the T Tauri component.

Are these sources descendants of HAeBes? Under the assumption that magnetospheric accretion in HAeBes is just a

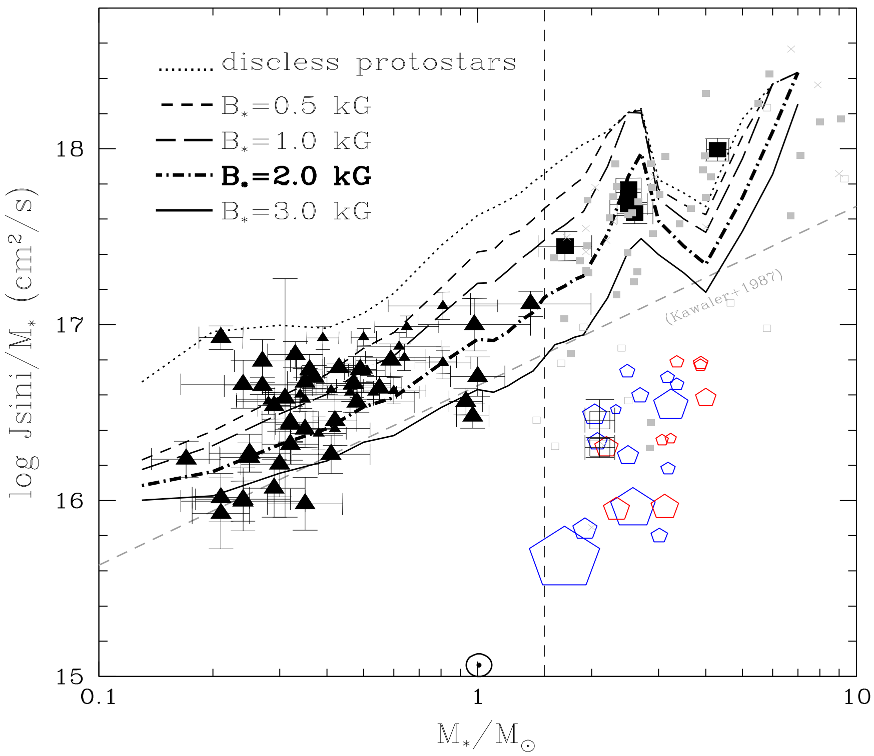

Figure 18. Angular momentum as a function of mass for TTs in the σ Orionis cluster (triangles) and HAeBes in OB1 (rectangles in black). The binary system HIP25258 is indicated with empty rectangles. TTs with active accretion are plotted with large triangles in black, while nonaccretors are small triangles. As complementary data for HAeBes, we included the sample studied by Alecian et al. (2013) with rectangles in gray, with open symbols representing binaries and crosses limit values. The dashed gray line represents the expected behavior for normal stars on the main sequence. Pentagons correspond to the sample of Ap/Bp stars of Aurière et al. (2007), with symbol sizes proportional to the dipolar field strengths reported by the authors. Symbols in blue correspond to Ap stars younger than 10 Myr, whereas whereas older stars, ranging from 10 Myr up to $\sim$300 Myr, are indicated in red. Tracks (in black with different line styles) represent a snapshot of angular momentum at 3 Myr for several magnetic field configurations, assuming that magnetic interaction between the protostar and its surrounding accretion disk started at the birthline (see the text). The vertical dashed line represents the boundary between TTs and HAeBes. The angular momentum of the Sun is assumed to be 10^{15} cm^2 s^{-1} for comparison purposes.

scaled version of that in TTs, we find this probable. If we assume that, at 3 Myr, magnetic fields in HAeBes have already formed via merging (Ferrario et al. 2009), then the stellar angular momentum can be transferred outward through outflows in the form of winds and magnetic interaction with the disk, if any. Wind torques could be applied onto the star up to the main sequence and beyond. By analyzing the computed ages for the Ap/Bp sample, we find that the majority are younger than 10 Myr (blue pentagons), suggesting that the merging scenario seems compatible with the fact that the loss of angular momentum must occur very early during the PMS phase (North 1998). We find that around $\sim 4.6 \times 10^{17}$ cm^2 s^{-1} of specific angular momentum must be lost in a few hundred Myr, from the HAeBes phase to Ap/Bp. HAeBes have larger J/M's than do Ap/Bp by a factor of 12 for the faster group, and almost 80 for the slowest rotating but highly magnetic Ap/Bp one.

Compared with normal (nonmagnetic) stars on the upper main sequence, Ap/Bp are slow rotators. From Figure 18 we can easily see that specific angular momentum for the faster group of Ap/Bp stars is about 25% of that for stars of similar spectral type (Kawaler 1987) and on the main sequence, and about 10% in the case of highly magnetic Ap /Bp stars.

8. Summary and Conclusions

Based on a sample of young stellar objects belonging to the molecular complex of star-forming regions in Orion, we computed $v \sin i$ values for 73 TTs and 6 HAeBes using two independent methods through a careful analysis of high-resolution spectra obtained with FIES and Hectochelle instruments. Radial velocities, visual extinction values, masses, radii, and ages were also computed. Radial and rotational projected velocities obtained from FIES spectra are in agreement with previous studies (Alecian et al. 2013; Fairlamb et al. 2015). For our HAeBes sample we obtain a median value of $\langle v \sin i \rangle = (115 \pm 9)$ km s^{-1}. Rotational velocities for the σ Orionis cluster using Hectochelle are independent of the implemented method (CCF and Fourier) under the uncertainties of each one.

We visually inspect the residual line profiles of HAeBes, finding evidence of accretion and winds; in particular HIP26955 is a star that displays PC profiles in all Balmer lines, significant [O I] 6300 Å emission, and a large infrared [3.4–2.2] μm WISE excess. While most prominent emission lines in all HAeBes show complex profiles with red, central, and blueshifted absorption features, and all of them exhibit Balmer excesses, only HIP26955 exhibits forbidden line emission in [O I]. These characteristics make it an excellent candidate for testing the magnetospheric accretion model.

With the aid of a rotational model, we investigated the trends in the $v \sin i$ versus mass diagram for masses between 0.1 $M_\odot$ and 7.0 $M_\odot$ when changes in accretion rates, magnetic field, and disk durability are included. The model includes a variable lifetime for the gas in the disk that marks the end of any torque acting on the star. It is assumed that accreting stars rotate as solid bodies and that they regulate their angular momentum through stellar winds powered by accretion. We adopted a uniform stellar dipolar field with constant strength B_*. For intermediate-mass stars we suppose that this field originated during the fully convective phase and has survived since (Wade et al. 2007).

By assuming that TTs and HAeBes are surrounded by gaseous disks during the first 3 Myr after the birthline, the best fit to the data was obtained for $B_* = 2.0$ kG. For this particular case, we obtained a set of relationships between stellar angular momentum and mass for different disk lifetimes ranging from diskless stars to stars with long-lived disks. We used these relationships, together with the Kawaler law, to estimate the amount of specific angular momentum that must be lost during the contraction toward the main sequence. On one hand, our results predict that HAeBes stars must lose angular momentum by a factor of ~3.2, equivalent to an amount of specific angular momentum equal to $\sim 3.2 \times 10^{17}$ cm^2 s^{-1}. On the other hand, $\langle J/M \rangle$ in TTs is larger by a factor of 5/2 than in stars on the main sequence.

We complemented our $\langle J/M \rangle$ values for HAeBes with those for the sample from Alecian et al. (2013) in order to compare our models with observed data of a particular sample of Ap/Bp stars analyzed by Aurière et al. (2007). We find that specific angular momentum must be lost by a factor of between 12 and 80 from HAeBes to Ap/Bp stars, depending on the intensity of the dipolar field.

Although detailed phenomena of TTs and HAeBes, such as stellar and disk inclination, disk photoevaporation, complex topologies of magnetospheres, and other factors, are not considered, the model presented here, based on simple assumptions, is extremely useful for testing the impact of rotation on distinct physical stellar parameters during the evolution of young stellar objects over a wide range of spectral types. However, the results obtained for the angular momentum in HAeBes do not explain the low rotation rates of Ap/Bp stars.

We thank the anonymous referee for providing many insightful comments. This research has been supported in part by observations made with the Nordic Optical Telescope, operated by the Nordic Optical Telescope Scientific Association at the Observatorio del Roque de los Muchachos, La Palma, Spain, of the Instituto de Astrofisica de Canarias. G.P. acknowledges support from UN (project HERMES 45442). J.H. acknowledges support from the National Research Council of México (CONACyT) project No. 86372 and the PAPIIT UNAM projects IA102921 and IN103320. E.M.M. acknowledges the receipt of the grant from the Abdus Salam International Centre for Theoretical Physics, Trieste, Italy. C.R.Z. acknowledges support from project CONACYT CB2018 A1-S-9754, México. A.R.L. acknowledges financial support provided in Chile by Comisión Nacional de Investigación Científica y Tecnológica (CONICYT) through the FONDECYT project 1170476 and by the QUIMAL project 130001.

ORCID iDs

Giovanni Pinzón https://orcid.org/0000-0001-9147-3345
Jesús Hernández https://orcid.org/0000-0001-9797-5661
Javier Serna https://orcid.org/0000-0001-7351-6540
Ezequiel Manzo-Martínez https://orcid.org/0000-0001-6647-862X
Alexandre Roman-Lopes https://orcid.org/0000-0002-1379-4204
Carlos G. Román-Zúñiga https://orcid.org/0000-0001-8600-4798
Yeisson Osorio https://orcid.org/0000-0001-5832-6933

References

Abt, H. A. 1979, ApJ, 230, 485
Ahuir, J., Brun, A. S., & Strugarek, A. 2020, A&A, 635, A170
Alecian, E., Catala, C., Wade, G. A., et al. 2008, MNRAS, 385, 391
Alecian, E., Wade, G. A., Catala, C., et al. 2009, MNRAS, 400, 354
Alecian, E., Wade, G. A., Catala, C., et al. 2013, MNRAS, 429, 1001
Armitage, P. J., & Clarke, C. J. 1996, MNRAS, 280, 458
Aurière, M., Wade, G. A., Silvester, J., et al. 2007, A&A, 475, 1053
Bailer-Jones, C. A. L. 2015, PASP, 127, 994
Bell, C. P. M., Naylor, T., Mayne, N. J., Jeffries, R. D., & Littlefair, S. P. 2013, MNRAS, 434, 806
Berger, E. 2006, ApJ, 648, 629
Beristain, G., Edwards, S., & Kwan, J. 2001, ApJ, 551, 1037
Boehm, T., & Catala, C. 1994, A&A, 290, 167
Bouvier, J. 2013, in Role and Mechanisms of Angular Momentum Transport During the Formation and Early Evolution of Stars Vol. 62 ed. P. Hennebelle & C. Charbonnel (Les Ulis: EAS Publications), 143
Briceño, C., Calvet, N., Hernández, J., et al. 2019, AJ, 157, 85
Briquet, M., Korhonen, H., González, J. F., Hubrig, S., & Hackman, T. 2010, A&A, 511, A71
Browning, M. K. 2008, ApJ, 676, 1262
Cabrit, S. 2007, in IAU Symp. 243, Star-Disk Interaction in Young Stars, ed. J. Bouvier & I. Appenzeller (Cambridge: Cambridge Univ. Press), 203
Calvet, N., Muzerolle, J., Briceño, C., et al. 2004, AJ, 128, 1294
Cardelli, J. A., Clayton, G. C., & Mathis, J. S. 1989, ApJ, 345, 245
Carroll, J. A. 1933, MNRAS, 93, 478
Castelli, F., Hubrig, S., Järvinen, S. P., & Schöller, M. 2020, MNRAS, 491, 2010
Cauley, P. W., & Johns-Krull, C. M. 2014, ApJ, 797, 112
Cauley, P. W., & Johns-Krull, C. M. 2015, ApJ, 810, 5
Chen, P. S., Shan, H. G., & Zhang, P. 2016, NewA, 44, 1
Cody, A. M., & Hillenbrand, L. A. 2010, ApJS, 191, 389
Coelho, P., Barbuy, B., Meléndez, J., Schiavon, R. P., & Castilho, B. V. 2005, A&A, 443, 735
Collier Cameron, A., Campbell, C. G., & Quaintrell, H. 1995, A&A, 298, 133
Corcoran, M., & Ray, T. P. 1997, A&A, 321, 189
Cranmer, S. R. 2008, ApJ, 689, 316
de Bruijne, J. H. J., & Eilers, A. C. 2012, A&A, 546, A61
Díaz, C. G., González, J. F., Levato, H., & Grosso, M. 2011, A&A, 531, A143
Dobler, W., Stix, M., & Brandenburg, A. 2006, ApJ, 638, 336
Donehew, B., & Brittain, S. 2011, AJ, 141, 46
Dotter, A. 2016, ApJS, 222, 8
Duflot, M., Figon, P., & Meyssonnier, N. 1995, A&AS, 114, 269
Fairlamb, J. R., Oudmaijer, R. D., Mendigutía, I., Ilee, J. D., & van den Ancker, M. E. 2015, MNRAS, 453, 976
Ferrario, L., Pringle, J. E., Tout, C. A., & Wickramasinghe, D. T. 2009, MNRAS, 400, L71
Gaia Collaboration, Brown, A. G. A., Vallenari, A., et al. 2021, A&A, 649, A1
Gallet, F., & Bouvier, J. 2013, A&A, 556, A36
Gallet, F., & Bouvier, J. 2015, A&A, 577, A98
Garaud, P. 2020, ApJ, 901, 146
Gomez, A. E., Luri, X., Grenier, S., et al. 1998, A&A, 336, 953
Hartigan, P., Edwards, S., & Ghandour, L. 1995, ApJ, 452, 736
Hartmann, L., Avrett, E., & Edwards, S. 1982, ApJ, 261, 279
Hartmann, L., Calvet, N., Gullbring, E., & D'Alessio, P. 1998, ApJ, 495, 385
Hartmann, L., Herczeg, G., & Calvet, N. 2016, ARA&A, 54, 135
Hartmann, L., Hewett, R., Stahler, S., & Mathieu, R. D. 1986, ApJ, 309, 275
Hartmann, L., & Stauffer, J. R. 1989, AJ, 97, 873
Hayashi, M. R., Shibata, K., & Matsumoto, R. 1996, ApJL, 468, L37
Herbst, W., Bailer-Jones, C. A. L., Mundt, R., Meisenheimer, K., & Wackermann, R. 2002, A&A, 396, 513
Hernández, J., Calvet, N., Hartmann, L., et al. 2005, AJ, 129, 856
Hernández, J., Calvet, N., Perez, A., et al. 2014, ApJ, 794, 36
Hernández, J., Hartmann, L., Megeath, T., et al. 2007, ApJ, 662, 1067
Hillenbrand, L. A., Strom, S. E., Vrba, F. J., & Keene, J. 1992, ApJ, 397, 613
Hone, E., Kraus, S., Kreplin, A., et al. 2017, A&A, 607, A17
Hosokawa, T., & Omukai, K. 2009, ApJ, 691, 823
Hubrig, S., Carroll, T. A., Scholler, M., & Ilyin, I. 2015, MNRAS, 449, L118

Hubrig, S., Ilyin, I., Schöller, M., et al. 2014, in Physics at the Magnetospheric Boundary Vol. 64 ed. E. Bozzo et al. (Les Ulis: EPJ), 08006
Hubrig, S., Mathys, G., Kurtz, D. W., et al. 2009a, MNRAS, 396, 1018
Hubrig, S., North, P., & Mathys, G. 2000, ApJ, 539, 352
Hubrig, S., Stelzer, B., Schöller, M., et al. 2009b, A&A, 502, 283
Hubrig, S., Yudin, R. V., Schöller, M., & Pogodin, M. A. 2006, A&A, 446, 1089
Iben, I. J. 1965, ApJ, 141, 993
Järvinen, S. P., Carroll, T. A., Hubrig, S., Ilyin, I., & Schöller, M. 2019, MNRAS, 489, 886
Jayawardhana, R., Coffey, J., Scholz, A., Brandeker, A., & van Kerkwijk, M. H. 2006, ApJ, 648, 1206
Kawaler, S. D. 1987, PASP, 99, 1322
Kochukhov, O., & Bagnulo, S. 2006, A&A, 450, 763
Kounkel, M., Covey, K., Moe, M., et al. 2019, AJ, 157, 196
Kounkel, M., Covey, K., Suárez, G., et al. 2018, AJ, 156, 84
Kurucz, R. L. 1979, ApJS, 40, 1
Leinert, C., Richichi, A., & Haas, M. 1997, A&A, 318, 472
Li, Z. Y., Banerjee, R., Pudritz, R. E., et al. 2014, in Protostars and Planets VI, ed. H. Beuther et al. (Tucson, AZ: Univ. Arizona Press), 173
MacGregor, K. B., & Brenner, M. 1991, ApJ, 376, 204
Manara, C. F., Testi, L., Natta, A., & Alcalá, J. M. 2015, A&A, 579, A66
Manoj, P., Bhatt, H. C., Maheswar, G., & Muneer, S. 2006, ApJ, 653, 657
Manzo-Martínez, E., Calvet, N., Hernández, J., et al. 2020, ApJ, 893, 56
Matt, S., & Pudritz, R. E. 2005, MNRAS, 356, 167
Matt, S., & Pudritz, R. E. 2008, ApJ, 678, 1109
Matt, S. P., Pinzón, G., de la Reza, R., & Greene, T. P. 2010, ApJ, 714, 989
Matt, S. P., Pinzón, G., Greene, T. P., & Pudritz, R. E. 2012, ApJ, 745, 101
Maucó, K., Hernández, J., Calvet, N., et al. 2016, ApJ, 829, 38
Mendigutía, I., Brittain, S., Eiroa, C., et al. 2013, ApJ, 776, 44
Mendigutía, I., Mora, A., Montesinos, B., et al. 2012, A&A, 543, A59
Moss, D. 1984, MNRAS, 207, 107
Moss, D. 1989, MNRAS, 236, 629
Moss, D. 1992, MNRAS, 257, 593
Muzerolle, J., D'Alessio, P., Calvet, N., & Hartmann, L. 2004, ApJ, 617, 406
Natta, A., Testi, L., & Randich, S. 2006, A&A, 452, 245
North, P. 1998, A&A, 334, 181
Pantolmos, G., Zanni, C., & Bouvier, J. 2020, A&A, 643, A129
Pecaut, M. J., & Mamajek, E. E. 2013, ApJS, 208, 9
Peña Ramírez, K., Béjar, V. J. S., Zapatero Osorio, M. R., Petr-Gotzens, M. G., & Martín, E. L. 2012, ApJ, 754, 30
Pérez-Blanco, A., Maucó, K., Hernández, J., et al. 2018, ApJ, 867, 116
Pöhnl, H., Paunzen, E., & Maitzen, H. M. 2005, A&A, 441, 1111
Pouilly, K., Bouvier, J., Alecian, E., et al. 2020, A&A, 642, A99
Press, W., Saul, T., William, V., & Brian, F. 2007, Numerical Recipes The Art of Scientific Computing (3rd ed.; Cambridge: Cambridge Univ. Press), 1
Ramanathan, A. S. 1954, AnAp, 17, 18
Rebull, L. M., Stauffer, J. R., Cody, A. M., et al. 2018, AJ, 155, 196
Reipurth, B., Bally, J., Aspin, C., et al. 2013, AJ, 146, 118
Rigliaco, E., Natta, A., Testi, L., et al. 2012, A&A, 548, A56
Rodríguez, L. F., Yam, J. O., Carrasco-González, C., Anglada, G., & Trejo, A. 2016, AJ, 152, 101
Romanova, M. M., Ustyugova, G. V., Koldoba, A. V., & Lovelace, R. V. E. 2005, ApJ, 635, L165
Rosen, A. L., Krumholz, M. R., & Ramirez-Ruiz, E. 2012, ApJ, 748, 97
Royer, F., Grenier, S., Baylac, M. O., Gómez, A. E., & Zorec, J. 2002, A&A, 393, 897
Sacco, G. G., Franciosini, E., Randich, S., & Pallavicini, R. 2008, A&A, 488, 167
Sicilia-Aguilar, A., Henning, T., & Hartmann, L. W. 2010, ApJ, 710, 597
Siess, L., Dufour, E., & Forestini, M. 2000, A&A, 358, 593
Simón-Díaz, S., Godart, M., Castro, N., et al. 2017, A&A, 597, A22
Tonry, J., & Davis, M. 1979, AJ, 84, 1511
Uzdensky, D. A., Königl, A., & Litwin, C. 2002, ApJ, 565, 1191
Vidotto, A. A., Gregory, S. G., Jardine, M., et al. 2014, MNRAS, 441, 2361
Vieira, S. L. A., Corradi, W. J. B., Alencar, S. H. P., et al. 2003, AJ, 126, 2971
Villebrun, F., Alecian, E., Hussain, G., et al. 2019, A&A, 622, A72
Vioque, M., Oudmaijer, R. D., Baines, D., Mendigutía, I., & Pérez-Martínez, R. 2018, A&A, 620, A128
Wade, G. A., Bagnulo, S., Drouin, D., Landstreet, J. D., & Monin, D. 2007, MNRAS, 376, 1145
Wheelwright, H. E., Oudmaijer, R. D., & Goodwin, S. P. 2010, MNRAS, 401, 1199
Wichittanakom, C., Oudmaijer, R. D., Fairlamb, J. R., et al. 2020, MNRAS, 493, 234
Wilson, A. 1969, MNRAS, 144, 325
Wolff, S. C., Strom, S. E., & Hillenbrand, L. A. 2004, ApJ, 601, 979
Zapatero Osorio, M. R., Béjar, V. J. S., Pavlenko, Y., et al. 2002, A&A, 384, 937
Zorec, J., & Royer, F. 2012, A&A, 537, A120